Variable density and anisotropic field-of-view for 3D Stack-of-Stars radial imaging

Tourais, Joao; Krishnamoorthy, Guruprasad; Smink, Jouke; Breeuwer, Marcel; Kouwenhoven, Marc

DOI
10.1007/s10334-025-01283-x

Publication date
2025

Document Version
Final published version

Published in
Magnetic Resonance Materials in Physics, Biology and Medicine

Magnetic Resonance Materials in Physics, Biology and Medicine
https://doi.org/10.1007/s10334-025-01283-x

RESEARCH ARTICLE

Variable density and anisotropic field-of-view for 3D Stack-of-Stars radial imaging

Joao Tourais[1,2,3] · **Guruprasad Krishnamoorthy**[1,2] · **Jouke Smink**[2] · **Marcel Breeuwer**[1,2] · **Marc Kouwenhoven**[2]

Received: 21 February 2025 / Revised: 5 July 2025 / Accepted: 15 July 2025

Abstract

Objective To develop a non-iterative method for applying elliptical field-of-view (FOV) to radial imaging and evaluate it for Stack-Of-Stars (SOS) with variable radial density in the k_z direction.

Materials and methods New analytic expressions were derived to compute the radial profile angles for an elliptical FOV with and without golden angle sampling. With a major-to-minor-axis FOV ratio of 1:0.5, anisotropic FOV and variable density SOS were evaluated, using point spread function analysis, phantom imaging, and in vivo pelvic imaging.

Results Compared with conventional SOS, elliptical density in k_z reduced scan time by 20%, while maintaining similar levels of radial aliasing artifacts. Anisotropic FOV reduced scan time by 31%, resulting in similar levels of radial aliasing artifacts at low undersampling for objects with matching in-plane anisotropy. Combining both techniques resulted in a 45% scan time reduction. Alternatively, when compared to conventional SOS using identical scan time, variable density and anisotropic FOV both displayed a lower level of radial aliasing artifacts, although for anisotropic FOV this effect was less pronounced at higher undersampling.

Discussion Variable density and anisotropic FOV can reduce scan time and/or reduce aliasing artifacts for SOS. The new analytical expressions for elliptical FOV will facilitate future studies on anisotropic FOV radial imaging.

Keywords Anisotropic FOV · Elliptical · Variable density · Radial imaging · Stack-Of-Stars

Introduction

Stack-Of-Stars (SOS) is a 3D acquisition using radial sampling in the in-plane direction (k_x-k_y) and Cartesian phase encoding in the through-plane direction (k_z). Radial imaging oversamples the k-space center, providing robustness against respiratory motion for abdominal, cardiac, and pelvic MRI, as demonstrated for 2D [1] and SOS [2–13]. SOS is often combined with golden angle sampling [14] or pseudo golden angle sampling [9–11], which further reduces motion-induced artifacts since consecutively acquired profiles are spaced by a large angle, resulting in an even distribution of motion effects over k-space [8–15]. To reduce scan time for SOS, conventional parallel imaging techniques [16, 17] and partial Fourier imaging [18] can be applied in the Cartesian slice direction. To further decrease scan time, radial undersampling may be applied, which effectively reduces the in-plane unaliased FOV (uFOV) size [19–21]. When using conventional radial reconstruction with phased array coils, a moderate undersampling generally does not lead to pronounced aliasing artifacts [21], while some applications like contrast-enhanced angiography allow high (up to eightfold) radial undersampling for SOS [4, 19].

With conventional SOS, the angular density of radial profiles is constant along the k_z axis. Peters et al. [22] proposed variable density sampling for SOS (VSOS), wherein the angular density decreases as a function of $|k_z|$. With identical scan times, the radial sampling density in the center of k_z is higher for VSOS than for conventional SOS, reducing the level of radial aliasing artifacts for VSOS. This was observed for VSOS using an (offset) cosine function [22] and a step

✉ Marc Kouwenhoven
marc.kouwenhoven@philips.com

1 Department of Biomedical Engineering, Eindhoven University of Technology, Eindhoven, The Netherlands

2 Department of MR R&D Clinical Science, Philips, Best, The Netherlands

3 Department of Imaging Physics, Delft University of Technology, Delft, The Netherlands

Published online: 15 October 2025

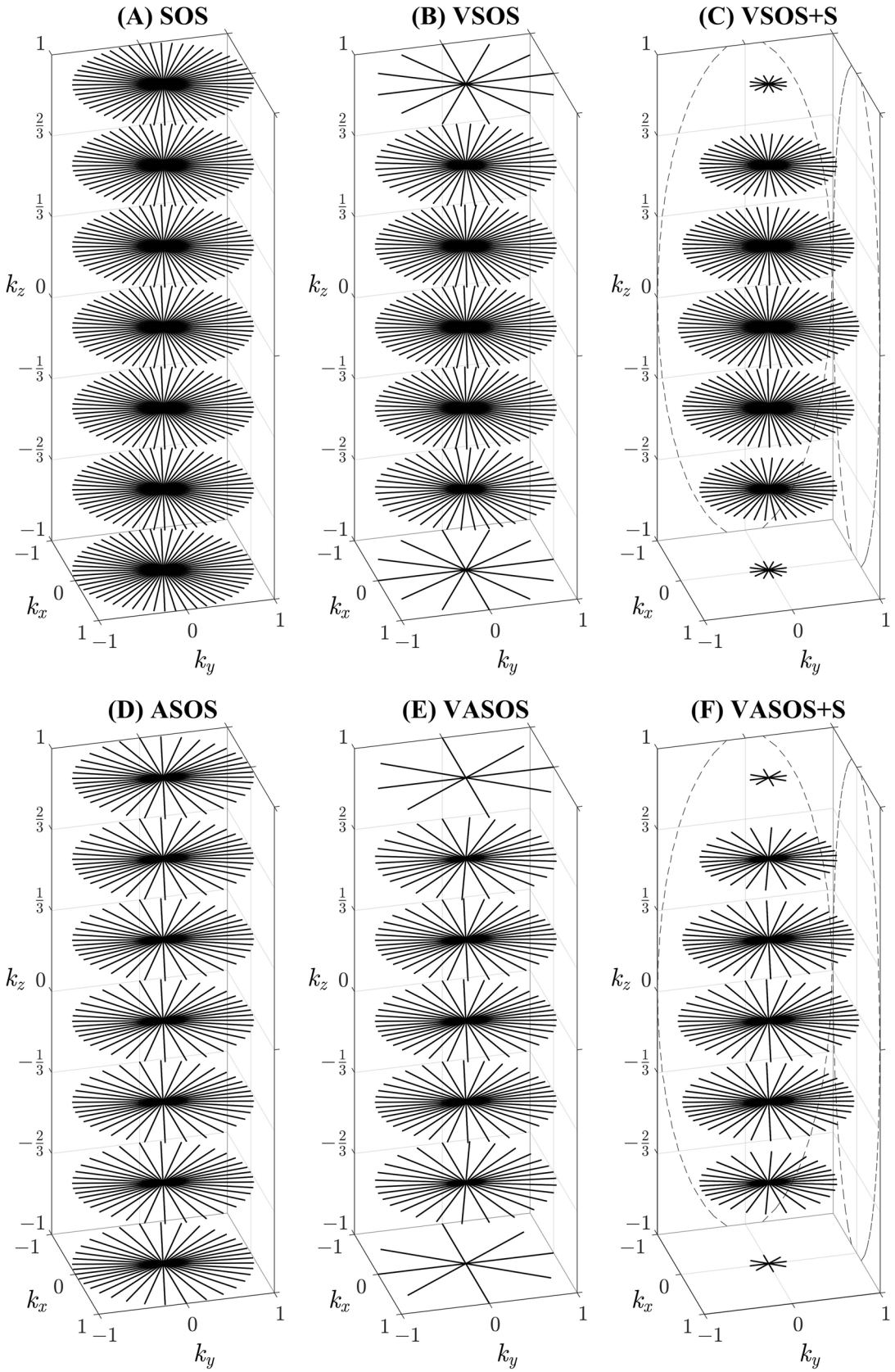
(A) SOS
(B) VSOS
(C) VSOS+S
(D) ASOS
(E) VASOS
(F) VASOS+S
k_z
k_x
k_y
1
$\frac{2}{3}$
$\frac{1}{3}$
0
$-\frac{1}{3}$
$-\frac{2}{3}$
−1

◂**Fig. 1** Distribution of radial profiles for six different 3D Stack-Of-Stars (SOS) sampling schemes. **A** Conventional SOS, **B** Variable density SOS (VSOS) without k-space shutter, **C** VSOS with k-space shutter (VSOS + S), **D** Anisotropic FOV SOS (ASOS), **E** Variable density and Anisotropic FOV SOS (VASOS) without k-space shutter and **F** VASOS with k-space shutter (VASOS + S). In **D**–**F**, an elliptical unaliased FOV was used, with an anisotropy $\eta = 0.5$ (minor-to-major-axis ratio), and the minor axis in the y direction. An elliptical function (Eqs. 22 and 23 with $N_z = 42$ and $f_p = 1$) was used for the variable density (**B**, **C**, **E**, **F**) and also for the k-space shutter (**C**, **F**). For improved visualization, the irregular spacing of golden angle sampling was not included, only a small number of k_z partitions and in-plane radial profiles are shown, and the length of the k_z axis is enlarged with respect to k_x and k_y

function [23]. With an identical radial sampling density in the center of k_z, VSOS results in shorter scan times than conventional SOS [24–26]. VSOS was also combined with golden angle sampling and compressed sensing reconstruction [27–29]. Despite these advantages, variable density is not yet commonly applied for SOS.

Pelvic and abdominal SOS imaging are commonly acquired in axial orientation [2, 3, 8–13]. However, an isotropic (circular) in-plane FOV may result in suboptimal sampling efficiency because in this axial plane, the pelvis/abdomen (including arms) generally has anisotropic dimensions. Scheffler et al. introduced anisotropic FOV for 2D radial imaging [30, 31]. Later, Larson et al. proposed an iterative method to obtain an anisotropic FOV with desired shapes for 2D and 3DPR (projection reconstruction) radial imaging [32]. This method was applied for 2D golden angle sampling (using additional interpolation) [33], for spiral phyllotaxis 3DPR [34], and for UTE 3DPR [35, 36]. By reducing the minor axis FOV, an anisotropic FOV can substantially reduce scan time. With low undersampling, this will not increase the level of radial aliasing for objects with matching anisotropic in-plane dimensions. This was demonstrated for 2D imaging, with a 50% scan time reduction for an elliptical FOV with an anisotropy ratio of 1:0.3 [32]. Alternatively, an anisotropic FOV can reduce the level of aliasing artifacts when compared with an isotropic FOV using identical scan time, as shown for 2D [32, 33] and 3DPR [32, 34]. This effect is more pronounced with low undersampling [32], but it has also been reported with high undersampling [32–34]. Despite these advantages, anisotropic FOV is not commonly applied for radial imaging, including SOS. This may be due to the relative complexity of the required iterative method, compounded by the additional interpolation needed for golden angle sampling. To our knowledge, only three studies have evaluated the benefits of anisotropic FOV for radial imaging [32–34].

While previous studies on radial anisotropic FOV have used cylindrical quadrature coils [32] and (phased array) surface coils [33, 34], the impact of receiver coil (element) size and uniformity on the effectiveness of anisotropic FOV for radial imaging remains unstudied. Similarly, while previous studies on SOS (with a circular FOV) have used phased array surface coils [2–4, 6–11, 19, 21], the effect of receiver coil (element) size on radial aliasing artifacts remains unstudied. We hypothesize that the level of radial aliasing in general, and the effectiveness of anisotropic FOV in particular may depend on the receiver coil.

In this study, we describe a new, non-iterative method to compute the radial profile angles for an elliptical FOV with and without golden angle sampling. This method is applied for Anisotropic FOV SOS (ASOS) and for the combination of Variable density and Anisotropic FOV SOS (VASOS). The effectiveness of VSOS, ASOS and VASOS is assessed through point spread function analysis, phantom imaging, and in vivo pelvic imaging. A phased array coil is used and compared with the quadrature body coil.

Materials and methods

Theory

Conventional radial imaging and unaliased field-of-view

In radial imaging, the unaliased FOV (uFOV) is determined by the Nyquist criterion [37]. Objects larger than the uFOV will cause aliasing manifested as streaking artifacts in the reconstructed image [21, 38, 39]. The in-plane uFOV for conventional SOS ($uFOV_c$) is defined like the uFOV for 2D radial imaging [19, 30]:

$$uFOV_c = \frac{FOV_r}{N_r} \cdot \frac{2}{\pi} \cdot N_{\theta c} \tag{1}$$

where FOV_r is the user-defined readout (and reconstruction) FOV size, N_r the number of corresponding readout samples (acquisition matrix size) on each radial profile, FOV_r/N_r the acquired spatial resolution, and $N_{\theta c}$ the number of acquired radial profiles (for each k_z partition). The uFOV has a circular shape with a diameter $uFOV_c$, and typically $uFOV_c \leq FOV_r$. For convenience, Eq. 1 can be rewritten as:

$$\rho = \frac{uFOV_c}{FOV_r} = \frac{2}{\pi} \cdot \frac{N_{\theta c}}{N_r} \tag{2}$$

where ρ is the radial sampling factor ($\rho = 1$ for full sampling, $\rho < 1$ for undersampling), and $\frac{1}{\rho}$ is the undersampling factor. The total number of acquired profiles is $N_{tc} = N_{\theta c} \cdot N_z$, where N_z is the number of acquired k_z partitions.

Variable density sampling for Stack-Of-Stars (VSOS)

Conventional SOS uses a constant density of radial profiles, where $N_{\theta c}$ does not depend on k_z (Fig. 1a). When a variable density $D_v(k_z)$ is applied for SOS (VSOS), the number of radial profiles $N_{\theta v}$ will vary over the k_z partitions (Fig. 1b), and $N_{\theta v}(k_z)$ can be written as:

$$N_{\theta v}(k_z) = N_{\theta c} \cdot D_v(k_z) \tag{3}$$

with $0 < D_v \leq 1$, and $D_v(0) = 1$. For clarity of notation, the parameter k_z is defined as being normalized $-1 \leq k_z \leq 1$. The variable density function $D_v(k_z)$ should decrease with $|k_z|$ but can have several shapes (e.g., elliptical, linear (diamond), step, etc.). Without variable density, $D_v(k_z) = 1$.

Optionally, a k-space shutter $S(k_z)$ can be applied, with radius S in the k_x-k_y plane. The number of remaining readout samples (as used for reconstruction) N_{rs} will then depend on k_z and can be expressed as:

$$N_{rs}(k_z) = N_r \cdot S(k_z) \tag{4}$$

with $0 < S \leq 1$, and $S(0) = 1$. FOV_r is not affected by the k-space shutter and remains constant over k_z.

When variable density is applied, including the k-space shutter (Fig. 1c), the corresponding uFOV ($uFOV_v$) can be obtained by combining Eqs. 1, 3 and 4:

$$uFOV_v(k_z) = uFOV_c \cdot \frac{D_v(k_z)}{S(k_z)} \tag{5}$$

where $uFOV_v(0) = uFOV_c$ is the nominal uFOV for VSOS. The shape of $S(k_z)$ can be chosen independently from $D_v(k_z)$, but in practice $S(k_z) \geq D_v(k_z)$. If no k-space shutter is applied, $S(k_z) = 1$.

The relative scan time T for VSOS (T_v) is defined as the inverse of the reduction factor (R) with respect to conventional SOS. $T_v = \frac{1}{R_v} = \frac{N_{tv}}{N_{tc}} = \frac{\overline{N}_{\theta v}}{N_{\theta c}} = \overline{D}_v$, where N_{tv} is the total number of VSOS profiles ($N_{tv} = \overline{N}_{\theta v} \cdot N_z$), $\overline{N}_{\theta v}$ the average number of profiles per k_z partition, and $\overline{D}_v$ the average variable density ($N_{\theta v}$ and D_v averaged over k_z). For a given, even function $D_v(k_z)$, T_v is a function of the partial Fourier factor in the slice direction f_p, and can be expressed as:

$$T_v(f_p) = \frac{1}{2f_p} \int_{-(2f_p-1)}^{1} D_v(k_z)\, dk_z \tag{6}$$

where $0 < T_v \leq 1$ and $0.5 < f_p \leq 1$. For example, a linear (diamond) density function $D_v(k_z) = 1 - |k_z|$ results in $T_v(f_p) = 2 - f_p - \frac{1}{2f_p}$, $T_v(1) = T_v\left(\frac{1}{2}\right) = \frac{1}{2}$, and $T_v\left(\frac{3}{4}\right) = \frac{7}{12}$ (Fig. 2a). Without variable density, $T_v(f_p) = 1$. The total number of acquired profiles with VSOS is $N_{tv}(f_p) = N_z \cdot N_{\theta c} \cdot T_v(f_p)$.

Anisotropic in-plane field-of-view

For SOS with an isotropic in-plane uFOV, the angular density of radial profiles may depend on k_z (when variable density is applied), but it is isotropic in the k_x-k_y plane (Figs. 1a–c and 3a). With an Anisotropic in-plane uFOV for SOS (ASOS), the angular density is also anisotropic (D_a) and depends on the angle θ in the k_x-k_y plane (Figs. 1d–f and 3c).

The anisotropic uFOV is denoted as $uFOV_a$, and its anisotropy η is defined as the minor-to-major-axis ratio. The major-to-minor-axis ratio is thus $1{:}\eta$ ($0 < \eta \leq 1$). The size of the major axis ($\theta = 0$, Fig. 3d) is assumed to be unaffected by η, so η is effectively the scale factor of the minor axis $\left(\theta = \frac{\pi}{2}\right)$. Following this definition, and using an isotropic circular uFOV as a reference for $uFOV_a$ ($uFOV_a = uFOV_c$ for $\eta = 1$), its major axis ($uFOV_a^+$) and minor axis ($uFOV_a^-$) can be defined as:

$$uFOV_a^+ = uFOV_c \tag{7}$$

$$uFOV_a^-(\eta) = uFOV_a^+ \cdot \eta \tag{8}$$

The anisotropic density D_a and the corresponding anisotropic $uFOV_a$ are a function of η and θ. $uFOV_a$ at angle θ is proportional to D_a at perpendicular angle $\theta + \frac{\pi}{2}$ [32] (Fig. 3), and can be expressed as:

$$uFOV_a(\eta, \theta) = uFOV_a^+ \cdot D_a\left(\eta, \theta + \frac{\pi}{2}\right) \tag{9}$$

$uFOV_a$ is assumed to be convex, and the density $D_a(\eta, \theta)$ is a π-periodic function ($D_a(\eta, \theta) = D_a(\eta, \theta + \pi)$). By definition, $uFOV_a^+ \equiv uFOV_a(\eta, 0)$, $uFOV_a^- \equiv uFOV_a\left(\eta, \frac{\pi}{2}\right)$, $D_a(\eta, 0) = \eta$ and $D_a\left(\eta, \frac{\pi}{2}\right) = 1$. For a circular uFOV, $D_a(1, \theta) = 1$, while for a square uFOV, $1 \leq D_a(1, \theta) \leq \sqrt{2}$.

The relative scan time for anisotropic FOV is defined as $T_a = \frac{1}{R_a} = \frac{N_{\theta a}}{N_{\theta c}} = \overline{D}_a$, where $N_{\theta a}$ is the number of anisotropic profiles (per k_z partition), and $\overline{D}_a$ the average anisotropic density (D_a averaged over θ). For a given density function $D_a(\eta, \theta)$, T_a can be expressed as:

$$T_a(\eta) = \frac{1}{\pi} \int_0^{\pi} D_a(\eta, \theta)\, d\theta \tag{10}$$

where $0 < T_a \leq \frac{4}{\pi}$, and $T_a(\eta) \geq \frac{2\sqrt{2}}{\pi} \cdot \eta$. For a diamond, circular, or square uFOV ($\eta = 1$), $T_a(1) = \frac{2\sqrt{2}}{\pi}$, 1, or $\frac{4}{\pi}$,

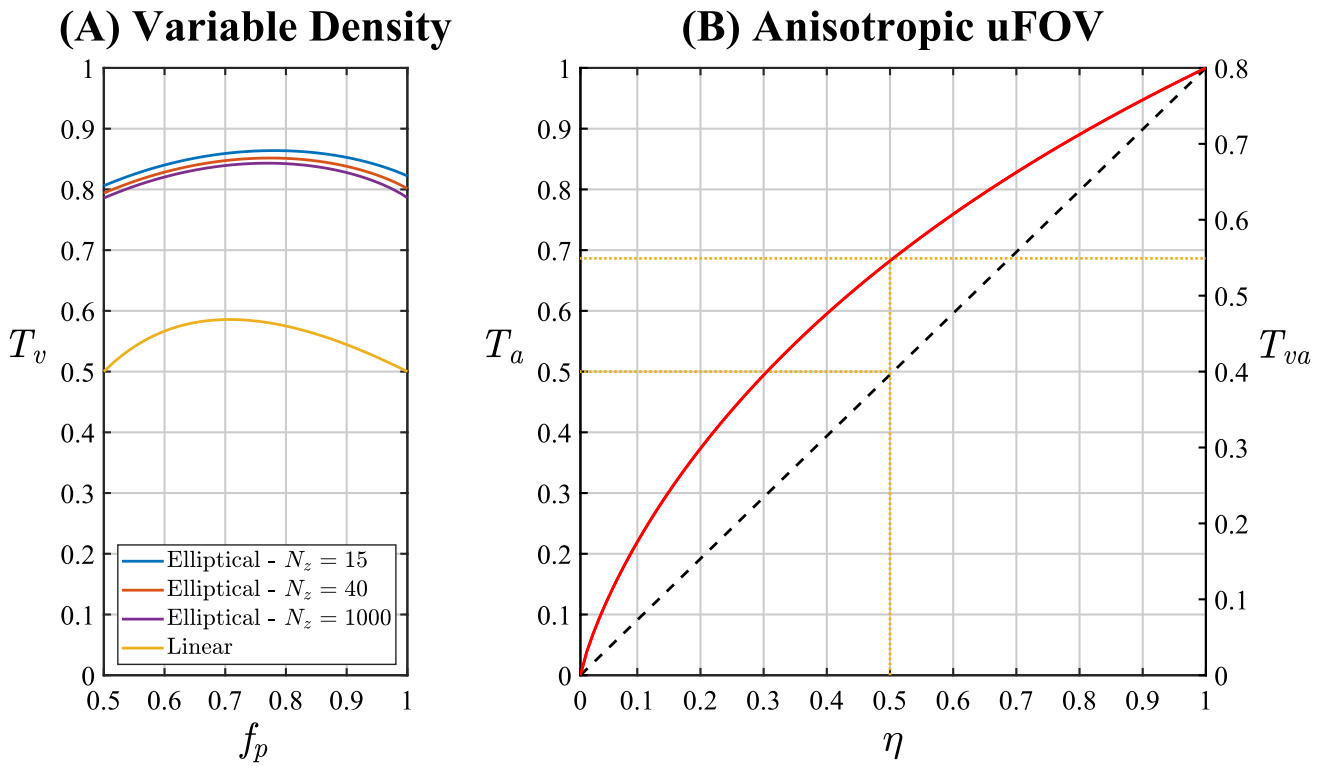

Fig. 2 Relative scan time ($T = 1/R$, where R is the reduction factor) for variable density, $T_v(f_p)$ and for anisotropic unaliased FOV (uFOV), $T_a(\eta)$. **A** Relative scan time T_v (Eq. 6) as a function of the partial Fourier factor (in the slice direction) f_p, for the elliptical variable density function D_v from Eq. 22, with the number of acquired k_z partitions N_z as parameter. For comparison, T_v is also shown (in yellow) for a linear (diamond) density function ($D_v(k_z) = 1 - |k_z|$). **B** Relative scan time T_a (Eq. 16) as a function of the uFOV anisotropy η (minor-to-major-axis ratio). The red solid curve is for radial imaging with an elliptical uFOV shape (Eq. 15), whereas the black dashed identity line is for Cartesian imaging with a rectangular (u) FOV ($T_a = FOV_y/FOV_r = \eta$). The yellow dotted lines show that with $\eta = 0.5$, the scan time reduction is 31% for radial ($T_a = 0.69$), while for Cartesian it is 50% ($T_a = 0.5$). The relative scan time for variable density and anisotropic uFOV combined is $T_{va} = T_v \cdot T_a$ (Eq. 14) and is shown on the right vertical axis of (**B**) for a representative value of $T_v = 0.8$ ($f_p = 1$, moderate N_z)

respectively. For an elliptical uFOV, $T_a \leq 1$, and $T_a(\eta) \geq \eta$ (Fig. 2b).

The number of radial profiles (per k_z partition) for anisotropic uFOV ($N_{\theta a}$) is a function of η:

$$N_{\theta a}(\eta) = N_{\theta c} \cdot T_a(\eta) \tag{11}$$

Variable density and anisotropic field-of-view Stack-Of-Stars (VASOS)

VASOS combines anisotropic in-plane uFOV with variable density (Fig. 1e) and (optional) additional k-space shutter (Fig. 1f). Similar to Eq. 5, the uFOV for VASOS ($uFOV_{va}$) can be written as:

$$uFOV_{va}(k_z, \eta, \theta) = uFOV_a(\eta, \theta) \cdot \frac{D_v(k_z)}{S(k_z)} \tag{12}$$

The nominal uFOV for VASOS is $uFOV_{va}(0, \eta, \theta) = uFOV_a(\eta, \theta)$, with major axis $uFOV^+_{va}(0) = uFOV^+_a$ and minor axis $uFOV^-_{va}(0, \eta) = uFOV^-_a(\eta) = uFOV^+_a \cdot \eta$.

Similar to Eq. 3, the number of radial profiles (for a given k_z partition) for VASOS ($N_{\theta va}$) can be expressed as:

$$N_{\theta va}(k_z, \eta) = D_v(k_z) \cdot N_{\theta a}(\eta) \tag{13}$$

As shown in the appendix, the relative scan time for VASOS (T_{va}) can be expressed as:

$$T_{va}(f_p, \eta) = T_v(f_p) \cdot T_a(\eta) \tag{14}$$

where $0 < T_{va} \leq \frac{4}{\pi}$. T_v and T_a are given by Eqs. 6 and 10, respectively. For an elliptical uFOV, $T_{va} \leq 1$. For a circular uFOV, and without variable density, $T_{va}(f_p, 1) = 1$.

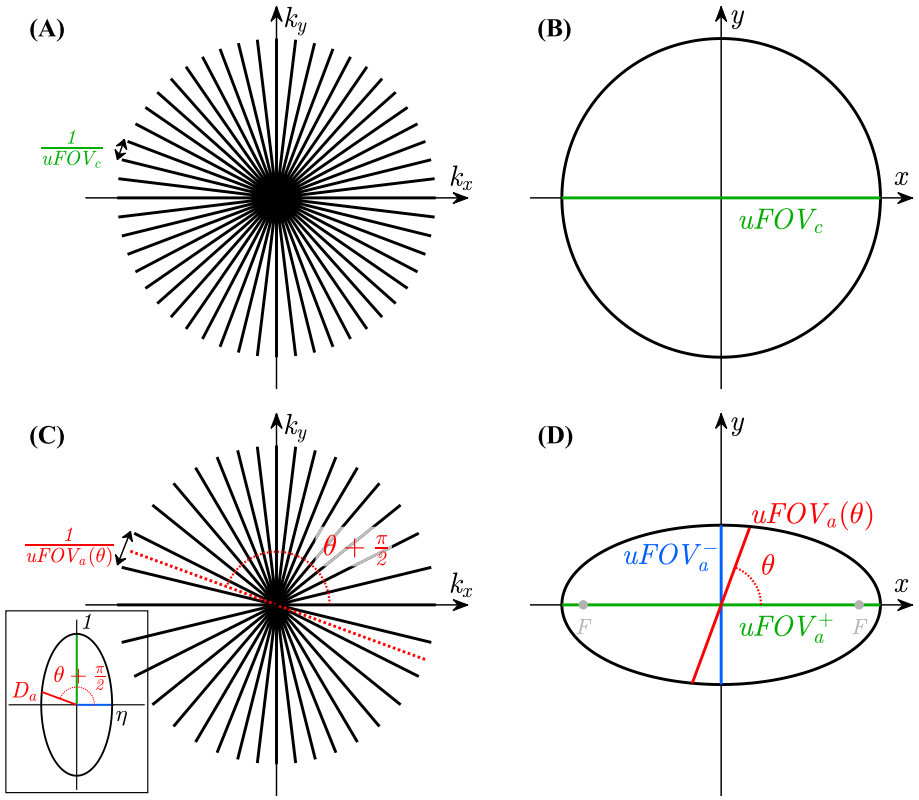

Fig. 3 Radial sampling density in k-space and resulting size and shape of the unaliased FOV (uFOV). **A** Radial sampling with isotropic angular density and **B** corresponding circular uFOV with diameter $uFOV_c$. **C** Radial sampling with anisotropic elliptical angular density D_a (shown as elliptical radius in the inset) and **D** corresponding elliptical uFOV with diameter $uFOV_a$ (Eq. 9), minor axis $uFOV_a^-$, and major axis $uFOV_a^+$ (uFOV anisotropy $\eta = uFOV_a^-/uFOV_a^+ = 0.5$, focal points F with eccentricity $\eta' = \sqrt{1-\eta^2} = 0.87$). Note that $uFOV_a(\theta) \propto D_a\left(\theta + \frac{\pi}{2}\right)$

Analytical expressions for elliptical field-of-view profile angles

For an elliptical $uFOV_a$ with anisotropy η, in line with Eqs. 7–9, the density D_a can be written as:

$$D_a(\eta,\theta) = \frac{\eta}{\sqrt{\cos^2(\theta) + \eta^2 \cdot \sin^2(\theta)}} \tag{15}$$

where $\eta \le D_a \le 1$, and $D_a(1,\theta) = 1$.

With Eqs. 10 and 15, the relative scan time $T_a(\eta)$ can be expressed analytically as:

$$T_a(\eta) = \eta \cdot \frac{2}{\pi} \cdot K\left(\eta'\right) \tag{16}$$

where $K(k)$ is the complete elliptic integral of the first kind, and $\eta' = \sqrt{1-\eta^2}$ is the elliptical eccentricity (usually referred to as "elliptic modulus" with symbol "k" in the context of elliptic integrals). $T_a(1) = 1$ $\left(K(0) = \frac{\pi}{2}\right)$, $T_a(0) = 0$ $\left(\lim_{\eta\to 0} \eta \cdot K\left(\eta'\right) = 0\right)$, and for $0 < \eta < 1$, $\eta < T_a(\eta) < 1$ (Fig. 2b).

By substituting Eqs. 2 and 16 in Eq. 11, $N_{\theta a}(\eta)$ for ASOS (and 2D imaging) with an elliptical uFOV can be expressed as:

$$N_{\theta a}(\eta) = N_r \cdot \rho \cdot \eta \cdot K\left(\eta'\right) \tag{17}$$

For VASOS with an elliptical uFOV, $N_{\theta va}\left(k_z,\eta\right)$ is obtained by substituting Eq. 17 in Eq. 13.

As shown in the appendix, for an elliptical FOV, the angle θ_i of the i^{th} radial profile can be expressed analytically by means of the Jacobi elliptic amplitude function $\text{am}(u,k)$ (Fig. 4a):

$$\theta_i = \text{am}\left(u_i,\eta'\right) \tag{18}$$

where $i = 0,1,2,\ldots,N_{\theta va}\left(k_z,\eta\right) - 1, \theta_0 = 0, 0 \le \theta_i < \pi$, and u_i is defined as:

$$u_i = \frac{i}{N_{\theta va}\left(k_z,\eta\right)} \cdot 2K\left(\eta'\right) \tag{19}$$

The values of θ_i and u_i depend on k_z and η ($\theta_i = \theta\left(i,k_z,\eta\right)$), but for simplicity, this is not included in the notation. For a circular uFOV ($\eta = 1$, $\eta' = 0$), Eqs. 18 and 19 reduce to $\theta_i = u_i = \frac{i}{N_{\theta v}(k_z)} \cdot \pi$, which is a uniform angular distribution for each k_z partition.

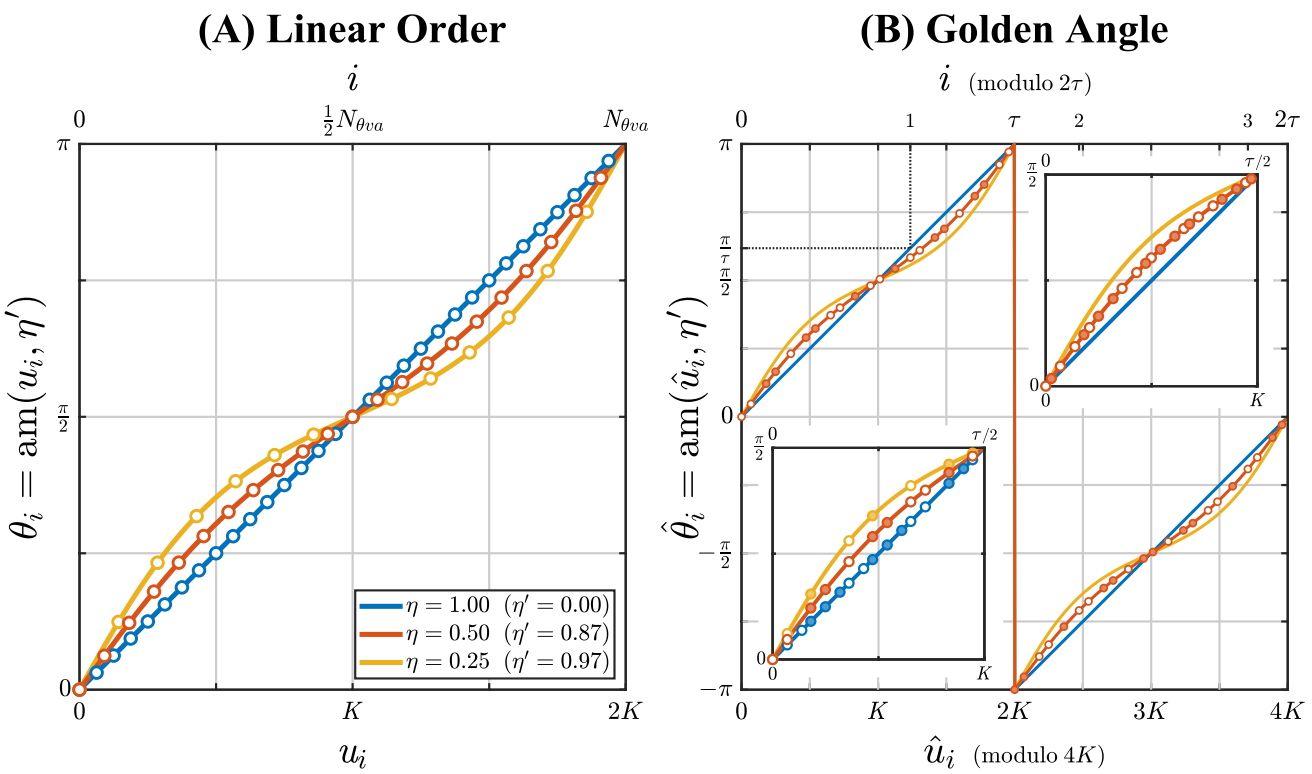

Fig. 4 The radial profile angle $\theta_i = \mathrm{am}(u_i, \eta')$ for an elliptical uFOV as a function of u_i (in units of $K(\eta')$), and as a function of the radial profile index i $(i = 0,1,\ldots,N_{\theta va} - 1)$. For demonstration, only a small number of radial profiles are used, displayed as dots, with $N_{\theta va} = 32, 22, 14$ for $\eta = 1, 0.5, 0.25$, respectively $(T_a(\eta) = 1, 0.69, 0.45)$. $\mathrm{am}(u_i, \eta')$ is the Jacobi elliptical amplitude function, $\eta' = \sqrt{1-\eta^2}$ is the elliptical eccentricity, and η is the uFOV anisotropy (minor-to-major-axis ratio). $K(\eta')$ is the complete elliptical integral of the first kind (for $\eta = 1$, $K(\eta') = \frac{\pi}{2}$). **A** θ_i, u_i and i for linear profile order (Eqs. 18 and 19) and pseudo golden angle (Eqs. 20 and 34). For each η, the dots are equidistant in u_i and i. Note that around $\theta_i = \frac{\pi}{2}$, the angular distance $(\Delta\theta_i)$ is similar for all η, while around $\theta_i = 0$ and π, $\Delta\theta_i \propto \frac{1}{\eta}$. **B** $\hat{\theta}_i$, $\hat{u}_i$ and i for golden angle sampling (Eqs. 20 and 21), where $\hat{\theta}_i$ (am) is limited (wrapped) from $-\pi$ to $+\pi$. The range for i (modulo 2τ) is shown from 0 to 2τ, where $i = 2\tau$ corresponds with $\hat{u}_i = 4K$, and τ is the golden ratio $\tau = \left(1+\sqrt{5}\right)/2 = 1.618$. The golden angle $(\Delta\hat{\theta}_{\Delta i=1} = \hat{\theta}_1$ for $\eta = 1)$ is $\frac{\pi}{\tau} = 0.618 \cdot \pi$ (black dotted line). The open dots represent the computed radial profile angles. For clarity, dots are only shown for $\eta = 0.5(N_{\theta va} = 22)$, and solid dots are added as duplicates of the open dots, shifted by π for $\hat{\theta}_i$ and shifted by $2K$ for $\hat{u}_i$ (or by τ for i). Note the irregular dot spacing (in $\hat{u}_i$ and i) with golden angle. The two insets zoom in on the range $0 - K$ $(0 - \frac{\tau}{2})$. The bottom left inset displays dots for all three η, showing the vertical alignment of the dots. The top right inset displays double the number of dots $(N_{\theta va} = 44)$, illustrating the reduced (but still irregular) spacing

Golden angle sampling

For golden angle sampling with VASOS and an elliptical uFOV, the profile angles $\hat{\theta}_i$ can also be expressed analytically, similar to Eq. 18:

$$\hat{\theta}_i = \mathrm{am}(\hat{u}_i, \eta') \tag{20}$$

where, using the quasi-periodicity of am $(\mathrm{am}(u + 2K(k), k) = \mathrm{am}(u, k) + \pi)$, $\hat{u}_i$ can be defined as:

$$\hat{u}_i = \frac{i}{\tau} \cdot 2K(\eta') \tag{21}$$

with $i = 0, 1, 2, \ldots, N_{\theta va}(k_z, \eta) - 1$, $\hat{\theta}_0 = 0$, and the golden ratio $\tau = \left(1+\sqrt{5}\right)/2$. Note that the effective range of $\hat{\theta}_i$ $(-\pi < \hat{\theta}_i \leq \pi)$ is twice that of θ_i, and that the values of $\hat{\theta}_i$ and $\hat{u}_i$ do not depend on k_z (Fig. 4b); only the number of profiles per k_z partition $(N_{\theta va})$ depends on k_z (if variable density is applied). For a circular uFOV $(\eta' = 0)$, Eqs. 20 and 21 reduce to $\hat{\theta}_i = \hat{u}_i = \frac{i}{\tau} \cdot \pi$, which are the profile angles for conventional golden angle sampling as described by Winkelmann et al. [14].

Methods

Elliptical variable density

For the variable density $D_v(k_z)$, an elliptical function was used:

$$D_v(k_z) = \sqrt{1 - (\lambda \cdot k_z)^2} \tag{22}$$

where $-1 \le k_z \le 1$, and

$$\lambda = \frac{N_z}{N_z + f_p} = \frac{N_z^+}{N_z^+ + \frac{1}{2}} \tag{23}$$

$D_v(0) = 1, 0 < D_v \le 1, \lambda \le 1$, f_p is the partial Fourier factor in the slice direction ($0.5 < f_p \le 1$), N_z the number of acquired k_z partitions, and $N_z^+ = N_z \cdot \frac{1}{2f_p}$ the number of partitions from $k_z = 0$ to 1. The factor λ is slightly less than 1 and is introduced to ensure that $D_v(k_z) > 0$ for $k_z = \pm 1$, which becomes relevant to preserve spatial resolution in the z direction when N_z is relatively small (e.g., for $N_z = 42$ and $f_p = 1$, $\lambda = 0.98$ and $D_v(\pm 1) = 0.2$, as shown in Figs. 1c and f).

The k-space shutter (S) used the same elliptical function as the variable density ($S(k_z) = D_v(k_z)$, Eq. 22).

An elliptically shaped $uFOV_a(\eta, \theta)$ was obtained by computing the profile angles θ_i for linear order sampling with Eqs. 18 and 19, and $\hat{\theta}_i$ for golden angle sampling with Eqs. 20 and 21. The number of profiles $N_{\theta va}(k_z, \eta)$ was computed with Eqs. 13 and 17, and subsequently rounded to an integer value. With variable density, $N_{\theta va}$ and θ_i need to be computed for each k_z partition, whereas the values of $\hat{\theta}_i$ need to be computed only once (for $i = 0,1,2,\ldots,N_{\theta va}(0,\eta) - 1$).

Point spread function

The point spread functions (PSF) were calculated in MATLAB (MathWorks, Natick, MA), which contains the $K(m)$ and $\mathrm{am}(u|m)$ functions ($m = k^2$). For VSOS and VASOS, the PSFs were computed without and with k-space shutter, and they were compared with the PSFs for conventional SOS and ASOS to assess the radial aliasing. The PSFs were computed with linear profile order, $N_r = 300$, $N_z = 84$, $f_p = 1$, $\rho = 1$, $\eta = 1$ ($N_{\theta c} = N_{\theta v}(0) = 471$ for SOS and VSOS), and $\eta = 0.5$ ($N_{\theta a}(0.5) = N_{\theta va}(0, 0.5) = 323$ for ASOS and VASOS).

MR acquisitions

Phantom and in vivo imaging were performed on a 3T Ingenia scanner (Philips, Best, Netherlands) with R5.7. VASOS acquisition and reconstruction were implemented on the MR scanner software platform. The radial profile angles $\hat{\theta}_i$ were computed on the fly during scan definition, using the C++Boost library v1.59.0 [40] to compute the required $K(k)$ and $\mathrm{am}(u,k)$. Since $\mathrm{am}(u,k)$ was not directly available in Boost, it was computed with the Jacobi elliptic function sn as:

$$\mathrm{am}'(u,k) = \arcsin(\mathrm{sn}(u,k)) \tag{24}$$

where $-\pi \le \mathrm{am}' \le \pi$. In-line radial reconstruction was used, with gridding [41, 42], density compensation [32, 37], phased array coil combination [43, 44], and coil sensitivity-related non-uniformity correction [15, 45]. The angular density compensation function (dcf) W_θ is given by:

$$W_\theta(k_z, \eta, \theta) = \frac{1}{D_{va}(k_z, \eta, \theta)} = \frac{1}{D_v(k_z) \cdot D_a(\eta, \theta)} \tag{25}$$

where $D_v(k_z)$ is given by Eq. 22 and $D_a(\eta, \theta)$ by Eq. 15.

VSOS, ASOS, and VASOS were compared with conventional SOS, and their radial aliasing artifact levels were

Table 1 Main parameters for SOS comparisons: uFOV anisotropy η, relative scan time T_{va}, relative radial sampling factor ρ', and related factors $\rho' \cdot T_{va}$, $\frac{1}{T_{va}}$, and $\frac{\eta}{T_{va}}$. $\rho' < 1$ is used for the retrospective undersampling of SOS_0, to obtain SOS'^{v}, SOS'^{a}, and SOS'^{va} (ρ' is proportional to $uFOV_c$ for SOS).

Sampling scheme	η	T_{va}	ρ'	$\rho' \cdot T_{va}$	$\frac{1}{T_{va}}$	$\frac{\eta}{T_{va}}$
SOS_0	1	1	1	1	1	1
VSOS	1	0.8	1	0.8	1.25	1.25
SOS'^{v}	1	1	0.8	0.8	1	1
ASOS	0.5	0.69	1	0.69	1.45	0.72
SOS'^{a}	1	1	0.69	0.69	1	1
VASOS	0.5	0.55	1	0.55	1.82	0.91
SOS'^{va}	1	1	0.55	0.55	1	1

$\rho' \cdot T_{va}$ is proportional to the net scan time (Eq. 29) and demonstrates that SOS'^{v}, SOS'^{a}, and SOS'^{va} have the same scan time as VSOS, ASOS, and VASOS, respectively. $\frac{1}{T_{va}}$ is the scale factor for the major axis uFOV of VSOS, ASOS, and VASOS, with respect to the uFOV of the corresponding SOS′ with the same scan time (SOS'^{v}, SOS'^{a}, and SOS'^{va}, respectively). Similarly, $\frac{\eta}{T_{va}}$ is the scale factor for the minor axis uFOV

qualitatively assessed. All acquisitions were repeated using the quadrature body (Q-Body) coil and a phased array surface coil (16-channel anterior array combined with the 12-channel built-in posterior array).

Conventional SOS was acquired in axial orientation using a 3D SOS RF-spoiled gradient echo with golden angle sampling. The scan parameters were: $FOV_r = 550$ mm, volume thickness = 180 mm, acquisition slice thickness = 3 mm, acquisition pixel size = 1.5×1.5 mm^2 ($N_r = 367$), reconstruction voxel size = $1.0 \times 1.0 \times 1.5$ mm^3, $f_p = 1$ (no partial Fourier), flip angle = 10°, bandwidth = 1000 Hz/pixel, and TE/TR = 1.45/3.6 ms. Adaptive RF shimming was applied [46, 47]. For the phased array coil acquisition, the radial sampling factor was $\rho = 0.7$, and SENSE factor = 2 (in slice direction, with $N_z = 42$), resulting in scan time = 1:01 min. For the Q-Body coil acquisition, a larger ρ ($\rho = 1.0$) was applied to prevent pronounced radial aliasing, and NSA = 2 was used to compensate for the inherently much lower SNR, resulting in scan time = 5:18 min. ASOS was acquired with $\eta = 0.5$ (minor-to-major-axis FOV ratio), but otherwise identical parameters, resulting in a 31% shorter scan time.

The golden angle sampling allowed retrospective undersampling, including variable density (Eq. 22). Hence, VASOS (with and without k-space shutter) and VSOS were reconstructed from ASOS and SOS, respectively, resulting in 20% fewer radial profiles.

The radial sampling factor ρ can be redefined as

$$\rho = \rho_0 \cdot \rho' \tag{26}$$

The baseline factor ρ_0 was varied in acquisitions, e.g. comparing different coils. The relative factor ρ' is 1.0 for VSOS, ASOS, VASOS, and conventional SOS (SOS_0). SOS'^{v}, SOS'^{a}, and SOS'^{va} were obtained by retrospectively undersampling SOS_0 to match the number of radial profiles of VSOS, ASOS, and VASOS, respectively, using $\rho' = T_{va}$. Table 1 contains the parameters η, T_{va}, and ρ' for all SOS variants.

To study the effect of receiver coil (element) size on radial aliasing artifacts, conventional SOS and ASOS were also acquired with a relatively small uFOV ($\rho = 0.4$) for both the phased array coil (NSA = 1) and the Q-Body coil (NSA = 5, to compensate for low SNR), and compared with the Q-Body coil acquisition with $\rho = 1.0$ (NSA = 2). To study the effect of radial undersampling on ASOS relative to conventional SOS, the phased array coil acquisitions using $\rho = 0.4$ and $\rho = 0.7$ were compared for ASOS and SOS.

All acquisitions were performed in phantom and in vivo. The phantom setup consisted of a cylindrical image quality phantom and a cylindrical uniform phantom placed side by side, resulting in a total axial cross-section of 190×390 mm^2. For the in vivo experiments, pelvic images were acquired in two healthy subjects, without applying respiratory compensation. Before scanning, written informed consent was obtained under a protocol approved by the ethics committee.

Results

Figure 1 shows the distribution of radial profiles for the different SOS sampling schemes (conventional SOS, ASOS, VSOS and VASOS, without and with k-space shutter). Conventional SOS has an angular density of radial profiles that is isotropic in the k_x-k_y plane and constant along the k_z axis (Fig. 1a). For VSOS and VASOS, the variable angular density decreases towards the periphery of k_z (Figs. 1b and e). For ASOS and VASOS, the angular density is anisotropic in the k_x-k_y plane (Figs. 1d–f). When the k-space shutter is applied for VSOS and VASOS, the distance between the radial profile tips is constant in k_z direction, for any given profile angle (Figs. 1c and f).

Figure 2a shows the relative scan time T_v for elliptical variable density (Eq. 22) as a function of the partial Fourier factor in the slice direction f_p, with the number of acquired k_z partitions (N_z) as parameter. Applying elliptical variable density resulted in a 20% reduction in scan time ($T_v = 0.8$) for $f_p = 1$ and a moderate N_z. Figure 2b shows the relative scan time T_a for an elliptical uFOV (Eq. 16) as a function of the uFOV anisotropy η. Using an elliptical uFOV with anisotropy $\eta = 0.5$ resulted in a 31% reduction in scan time ($T_a = 0.69$). Combining the elliptical variable density with the elliptical uFOV resulted in a 45% reduction in scan time for VASOS with $\eta = 0.5$ ($T_{va} = T_v \cdot T_a = 0.8 \cdot 0.69 = 0.55$).

Figure 5 shows the PSFs of the different SOS sampling schemes, demonstrating the resulting uFOV and level of radial aliasing artifacts. Conventional SOS (Fig. 5a) and ASOS (Fig. 5d) resulted in a clearly defined aliasing-free cylindroid uFOV. Applying variable density without k-space shutter resulted in an increased level of aliasing inside the nominal uFOV of VSOS (Fig. 5b) and VASOS (Fig. 5e). In the center of the nominal uFOV, a small cylindroid region remained aliasing-free (visible in the sagittal and coronal orientations), with in-plane dimensions determined by the lowest density $D_v(k_z = \pm 1)$. Outside the nominal uFOV, the level of aliasing was decreased compared with conventional SOS and ASOS. Applying the k-space shutter for VSOS (Fig. 5c) and VASOS (Fig. 5f) substantially reduced the level of aliasing artifacts inside the (nominal) uFOV, compared with VSOS and VASOS without shutter (Figs. 5b and e).

Figures 6, 7, and 8 compare the different SOS sampling schemes, using a phased array coil ($\rho_0 = 0.7$) and the Q-Body coil ($\rho_0 = 1.0$), for phantom and in vivo imaging. VSOS, ASOS, and VASOS showed similar aliasing artifact

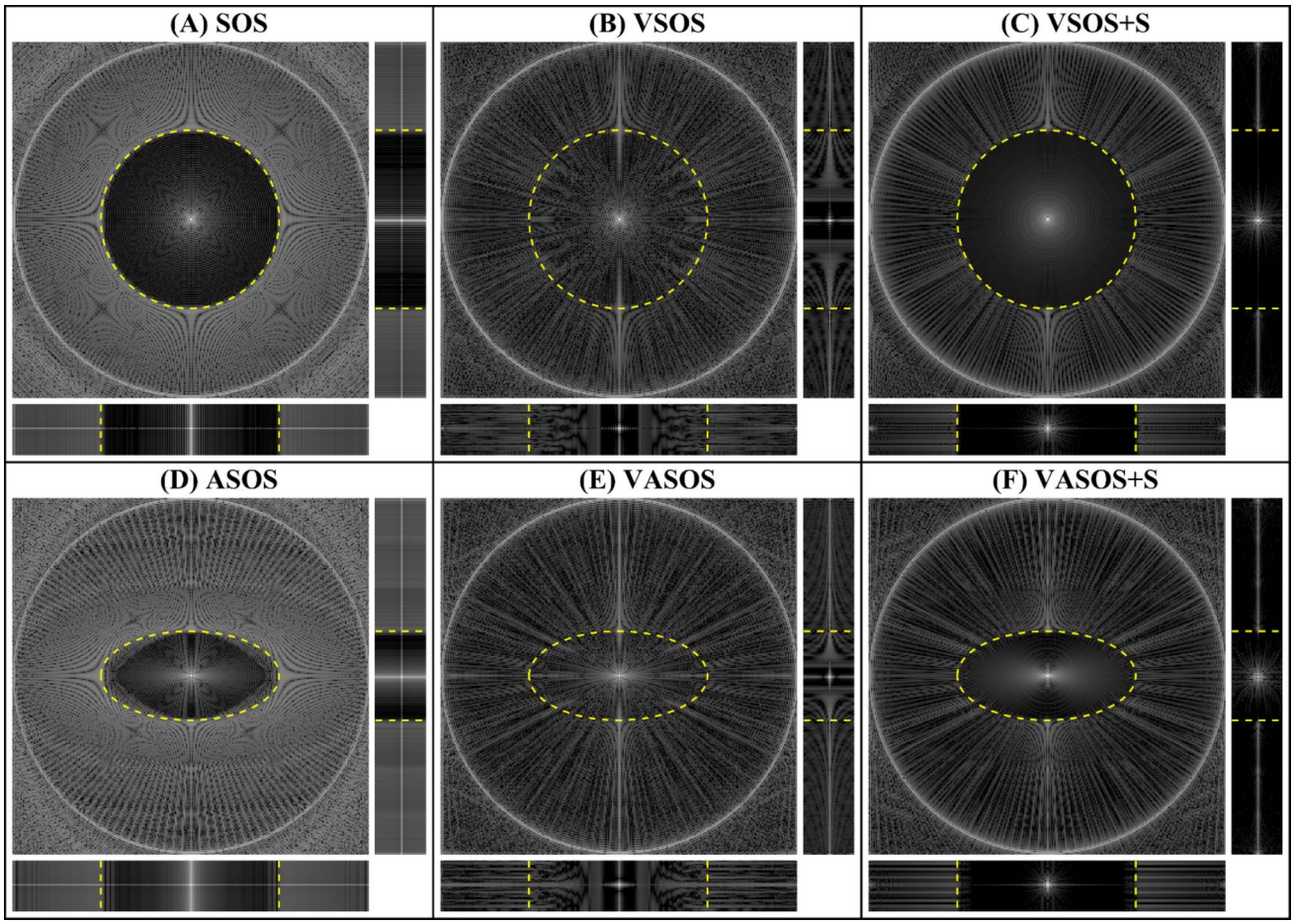

Fig. 5 Point Spread Functions (PSFs) for six different Stack-Of-Stars (SOS) schemes. **A** Conventional SOS, **B** Variable density SOS (VSOS) without k-space shutter, **C** VSOS with k-space shutter (VSOS + S), **D** Anisotropic FOV SOS (ASOS), **E** Variable density and Anisotropic FOV SOS (VASOS) without k-space shutter and **F** VASOS with k-space shutter (VASOS + S). For each SOS scheme, the central slices of the transverse (top left), sagittal (top right), and coronal (bottom) orientations are shown. The yellow dashed lines indicate the (nominal) unaliased FOV (uFOV). All PSFs are displayed on a logarithmic gray scale. VSOS (**B** and **C**), ASOS (**D**), and VASOS (**E** and **F**) require 20%, 31%, and 45% fewer profiles compared to conventional SOS (**A**), respectively

levels as conventional SOS (SOS_0) using the same (nominal, major axis) uFOV size, while requiring 20%, 31%, and 45% fewer profiles due to variable density, reduced minor axis uFOV, and both combined, respectively. VSOS, ASOS, and VASOS showed a lower level of radial aliasing artifacts compared with conventional SOS using the same scan time (SOS'^{v}, SOS'^{a}, and SOS'^{va}, with a 20%, 31% and 45% smaller uFOV than SOS_0, respectively). VASOS with k-space shutter (VASOS + S) showed similar aliasing artifact levels as VASOS without k-space shutter. All these results were observed for both the phased array coil and the Q-Body coil, although for the phased array coil, the effect of anisotropic FOV was less pronounced. Additionally, for all types of SOS sampling schemes, the phased array coil showed lower radial aliasing levels than the Q-Body coil, despite using a larger uFOV (ρ) for the latter.

Figure 9 shows the effect of radial undersampling on ASOS relative to conventional SOS, for the phased array coil. For $\rho = 0.7$, ASOS showed a similar level of artifacts as conventional SOS with the same (major axis) uFOV size (SOS_0), as already shown in Figs. 6–8, while for $\rho = 0.4$, ASOS showed a higher level of artifacts than SOS_0. For both $\rho = 0.7$ and $\rho = 0.4$, ASOS showed a reduced aliasing artifact level compared with conventional SOS using the same scan time (SOS'^{a}, with a 31% smaller uFOV than SOS_0). However, for ASOS with $\rho = 0.4$, this reduction in aliasing was less pronounced than for ASOS with $\rho = 0.7$.

Figure 10 shows the effect of receiver coil on radial aliasing. The phased array coil acquisitions showed a substantially lower level of aliasing than Q-Body coil acquisitions with the same uFOV, while showing a similar level of aliasing as the Q-Body coil acquisitions with a 2.5-fold larger uFOV.

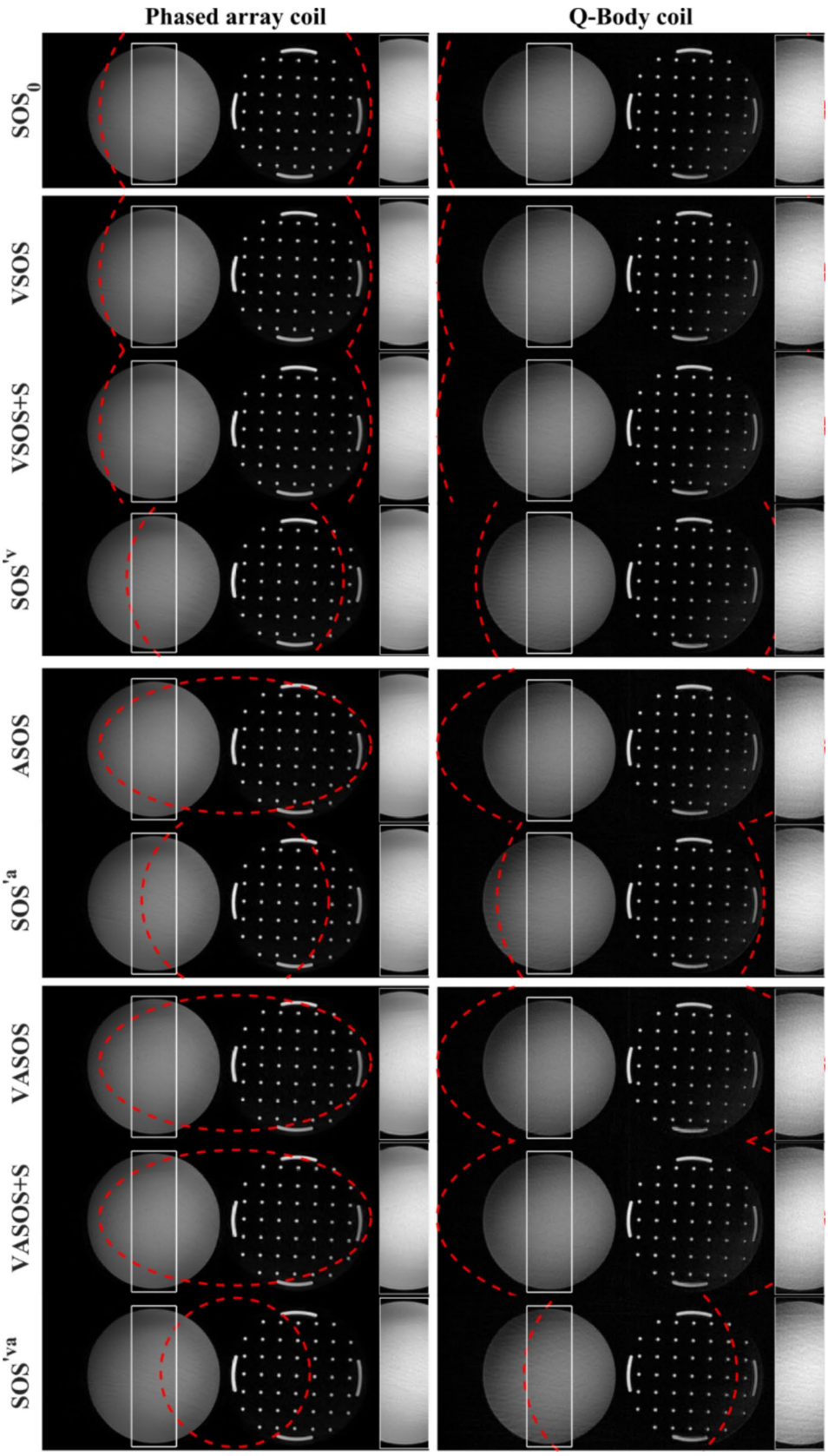

Fig. 6 Phantom images comparing conventional SOS, VSOS with (+S) and without k-space shutter, ASOS, VASOS, and VASOS + S using different unaliased FOV (uFOV) sizes and different coils. The red dashed lines indicate the shape and size of the uFOV. Compared with conventional SOS_0 (1st row), the scan times for VSOS (2nd and 3rd row), ASOS (5th row), and VASOS (7th and 8th row) were 20%, 31%, and 45% shorter, respectively, while using the same (nominal, major axis) uFOV size. Conventional SOS'^{v} (4th row), SOS'^{a} (6th row), and SOS'^{va} (9th row) had a 20%, 31% and 45% smaller uFOV (ρ') than SOS_0 and had an identical scan time as VSOS, ASOS, and VASOS, respectively. Phased array coil (left column, $\rho_0 = 0.7$) and Q-Body coil with 1.4-fold larger uFOV (right column, $\rho_0 = 1.0$). To better illustrate the aliasing artifacts, a region (white rectangle) is enlarged in the inset. Different techniques with the same relative scan time are grouped (separated by a horizontal white line)

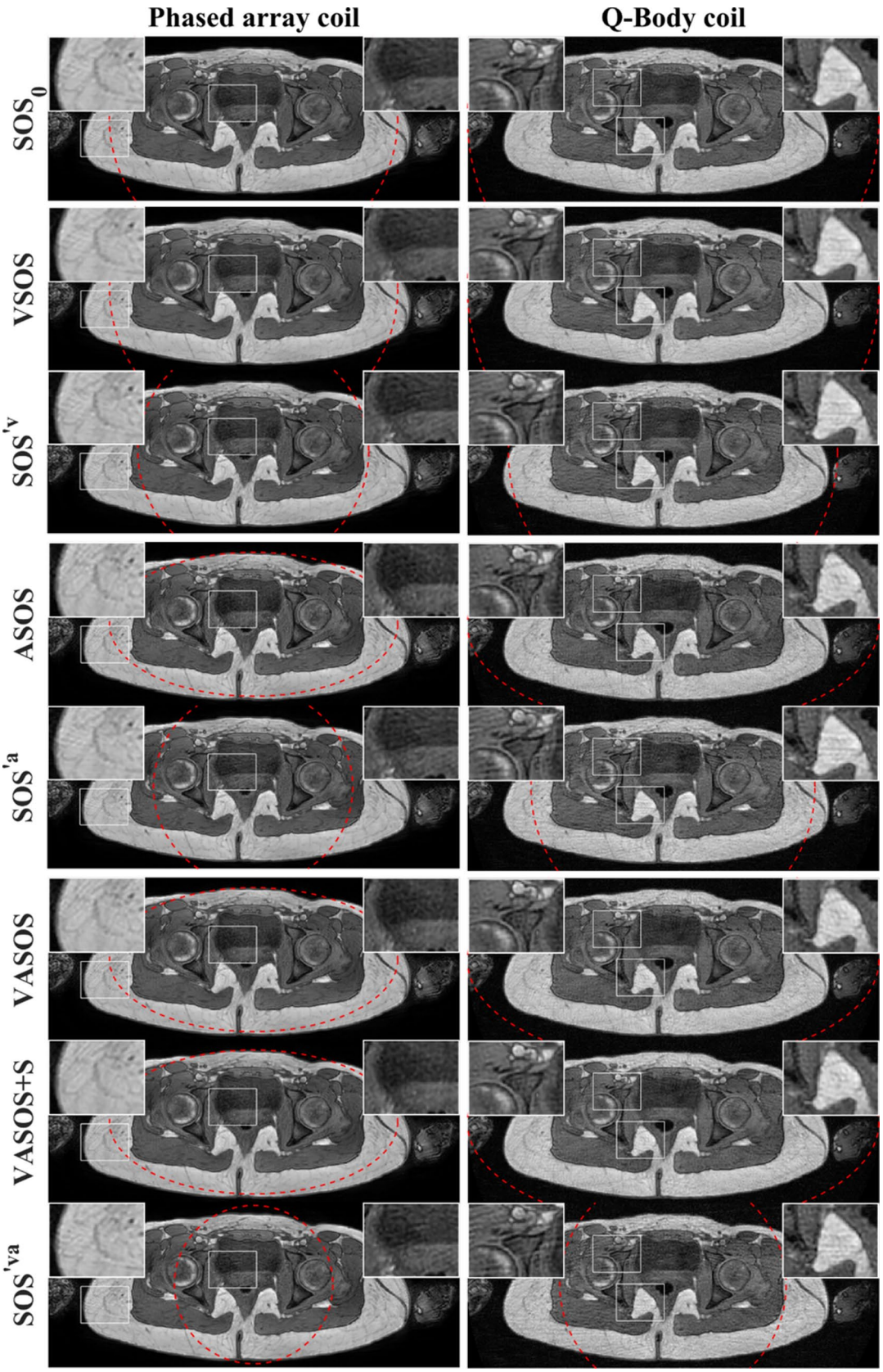
Phased array coil
Q-Body coil
SOS0
VSOS
SOS'v
ASOS
SOS'a
VASOS
VASOS+S
SOS'va

◂**Fig. 7** Pelvic images comparing conventional SOS, VSOS, ASOS, and VASOS with (+S) and without k-space shutter using different unaliased FOV (uFOV) sizes and different coils. The red dashed lines indicate the uFOV. Compared with conventional SOS_0 (1st row), the scan times for VSOS (2nd row), ASOS (4th row), and VASOS (6th and 7th row) were 20%, 31%, and 45% shorter, respectively, while using the same (nominal, major axis) uFOV size. Conventional SOS'^{v} (3rd row), SOS'^{a} (5th row), and SOS'^{va} (8th row) had a 20%, 31% and 45% smaller uFOV (ρ') than SOS_0 and had an identical scan time as VSOS, ASOS, and VASOS, respectively. Phased array coil (left column, $\rho_0 = 0.7$) and Q-Body coil with 1.4-fold larger uFOV (right column, $\rho_0 = 1.0$). To better illustrate the aliasing artifacts, certain regions (white rectangles) are enlarged in the inset. Different techniques with the same relative scan time are grouped (separated by a horizontal white line)

Discussion

Analytic expressions for elliptical uFOV profile angles

New, analytic expressions are proposed to compute the radial profile angles θ_i and the number of profiles $N_{\theta a}$ for an elliptical uFOV shape (Eqs. 17–19). These expressions offer a convenient alternative to the iterative method proposed by Larson et al. [32], although the latter is more general by allowing any convex uFOV shape.

The new analytic expressions also include the profile angles $\hat{\theta}_i$ for golden angle sampling with elliptical uFOV (Eqs. 20 and 21), eliminating the additional requirement for interpolation as described by Wu et al. [33]. Pseudo golden angle sampling [9–11] is also supported (Eqs. 20 and 34). Tiny golden angle sampling [48, 49] can be obtained by substituting τ in Eq. 21 or 34 with $\tau' = \tau + M - 1$, where $M = 1, 2, 3, \ldots$, with $M = 2$ being the complementary small golden angle sampling, and $M \geq 3$ the tiny golden angle sampling.

Besides SOS, the analytic expressions for an elliptical uFOV are also applicable for 2D and 3DPR.

Eqs. 17–21 and 34 use the complete elliptic integral of the first kind $K(k)$ and the Jacobi elliptic amplitude function $\mathrm{am}(u, k)$, which can be computed with many software libraries and platforms (e.g., C++ Boost, Python SciPy, MATLAB, and Mathematica).

Variable density

As shown in Fig. 2a, the elliptical variable density function (Eq. 22) allows a maximum scan time reduction of 21.5% $\left(T_v = \frac{\pi}{4}\right)$, if no partial Fourier is applied ($f_p = 1$) and if a large number of k_z partitions (N_z) is acquired. A moderate N_z, as used for phantom and in vivo imaging (with $f_p = 1$), resulted in a slightly smaller scan time reduction of 20% ($T_v = 0.8$). Other density functions can be applied (e.g., cosine [22], step [23], linear (diamond) [25]), which may achieve greater scan time reductions at the cost of increased aliasing for peripheral k_z partitions.

When variable density is applied without k-space shutter ($S(k_z) = 1$), the uFOV size depends on k_z and is proportional to the density function $D_v(k_z)$ (Eqs. 5 and 12) which decreases towards the periphery of k_z. This resulted in an increased aliasing artifact level inside the nominal uFOV of the PSF for VSOS compared with SOS (Fig. 5b vs a) and VASOS compared with ASOS (Fig. 5e vs d). As a result of this aliasing induced by variable density, the level of pseudo-noise slightly increased in phantom imaging (Fig. 6, VSOS vs SOS_0 and VASOS vs ASOS). When additionally, a k-space shutter is applied using the same function as the variable density ($S(k_z) = D_v(k_z)$), the uFOV no longer depends on k_z (Eqs. 5 and 12) and is equal to the nominal uFOV. This eliminated the aliasing induced by variable density in the PSF (Figs. 5c and f) and slightly reduced the pseudo-noise in phantom imaging (Fig. 6, VSOS + S and VASOS + S). Applying an elliptical k-space shutter produces a spheroid boundary in k-space, resulting in a more isotropic spatial resolution [50], similar to the spherical Stack-Of-Spirals trajectory [51, 52].

The PSF showed a reduced aliasing artifact level outside the nominal uFOV for VSOS and VASOS (Figs. 5b,c,e,f) compared with conventional SOS and ASOS (Figs. 5a,d). This reduction is due to the linear profile order as used for the PSF, which results in the nonalignment of profiles throughout k_z when combined with variable density, similar to the effect observed with rotated SOS [53].

Anisotropic FOV and scan time

As shown in Fig. 2b, for radial imaging with an anisotropic elliptical uFOV, the relative scan time T_a is non-linear with the FOV anisotropy η, and $T_a > \eta$ (for $\eta < 1$), while for Cartesian imaging, $T_a = \eta$ ($\eta = FOV_y/FOV_r$). Thus, the scan time reduction $(1 - T_a)$ for radial imaging is smaller than for Cartesian. For example, with $\eta = 0.5$, for radial imaging with an elliptical uFOV, scan time is reduced by 31% ($T_a = 0.69$) instead of 50% for Cartesian. By combining the elliptical uFOV with elliptical variable density, a higher scan time reduction of 45% ($T_{va} = T_v \cdot T_a = 0.55$) is obtained for VASOS.

Impact of coil (element) size

To evaluate the impact of coil (element) size on the aliasing level, conventional SOS and ASOS were acquired with a relatively small uFOV ($\rho = 0.4$) for both the Q-Body coil and the phased array coil (Fig. 10). The phased array coil showed a substantially lower level of aliasing artifacts than

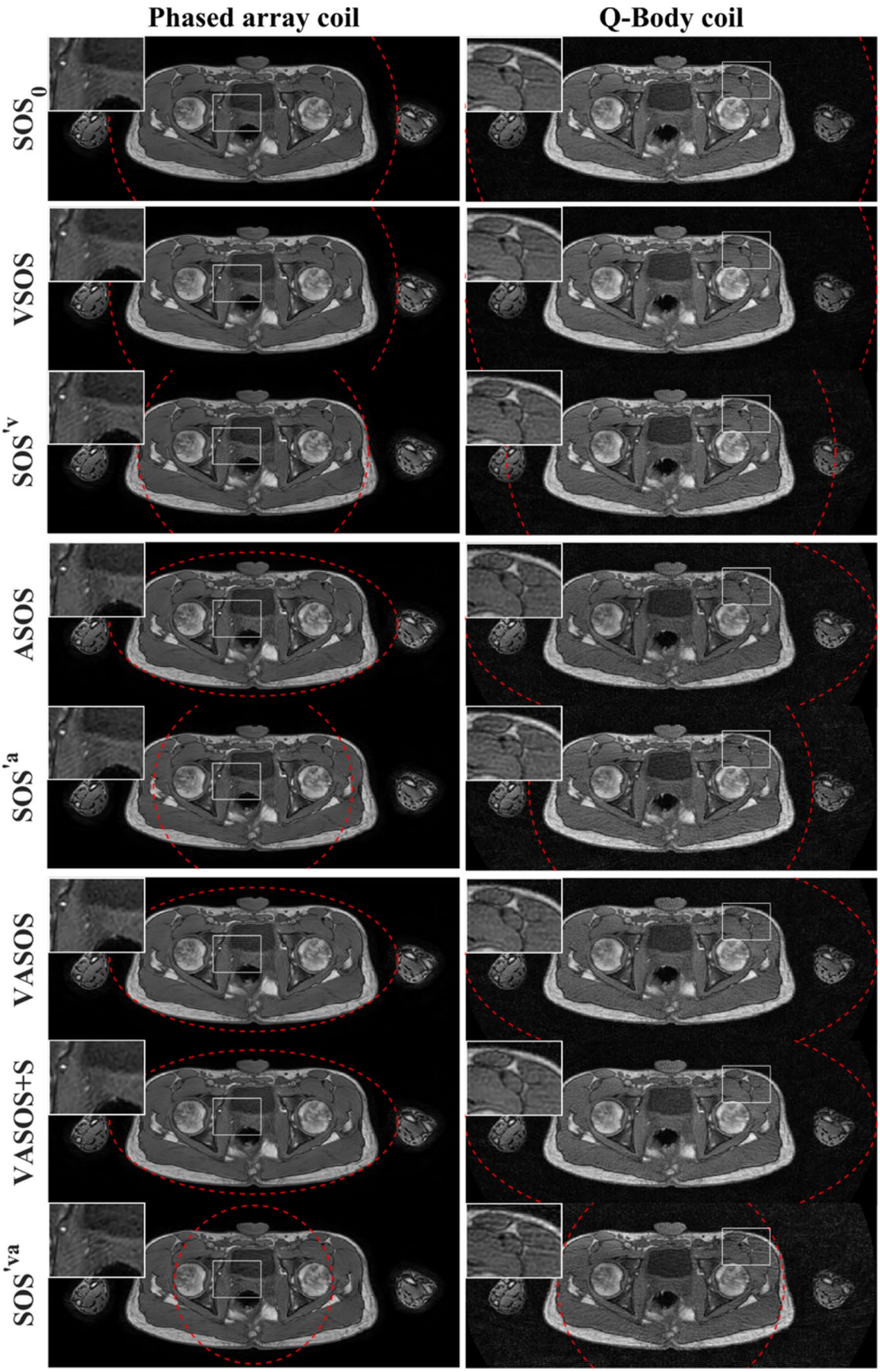
Phased array coil
Q-Body coil
SOS0
VSOS
SOS'v
ASOS
SOS'a
VASOS
VASOS+S
SOS'va

◂**Fig. 8** Pelvic images comparing conventional SOS, VSOS, ASOS, and VASOS with (+S) and without k-space shutter using different unaliased FOV (uFOV) sizes and different coils. The uFOV is indicated by red dashed lines. Compared with conventional SOS_0 (1st row), the scan times for VSOS (2nd row), ASOS (4th row), and VASOS (6th and 7th row) were 20%, 31%, and 45% shorter, respectively, while using the same (nominal, major axis) uFOV size. Conventional SOS'^{v} (3rd row), SOS'^{a} (5th row), and SOS'^{va} (8th row) had a 20%, 31% and 45% smaller uFOV (ρ') than SOS_0 and had an identical scan time as VSOS, ASOS, and VASOS, respectively. Phased array coil (left column, $\rho_0 = 0.7$) and Q-Body coil with a 1.4-fold larger uFOV (right column, $\rho_0 = 1.0$). To better illustrate the aliasing artifacts, a region (white rectangle) is enlarged in the inset. Different techniques with the same relative scan time are grouped (separated by a horizontal white line)

the Q-Body coil. This result contrasts with conventional Cartesian imaging (without parallel imaging), where aliasing artifacts with Q-Body and phased array coils are typically similar [54, 55]. Radial sampling uses a rotating readout gradient with oversampling, resulting in a relatively low level of aliasing artifacts for the images of each single element from the phased array coil, due to their relatively small size and corresponding sensitivity area. After coil combination, this results in a low aliasing artifact level in the final image. This is similar to the behavior of aliasing artifacts in Cartesian Parallel Imaging with Localized Sensitivity (PILS) [55, 56]. However, to obtain an aliasing-free image, PILS requires a uFOV smaller than the width of the coil element sensitivity and the knowledge of the coil element positions during reconstruction, which is not required for radial.

For each coil, VSOS, ASOS, and VASOS resulted in a lower radial aliasing artifact level compared with conventional SOS using identical scan time. As expected, the effect of variable density was independent of the used coil. However, the effect of anisotropic FOV was less pronounced with the phased array coil compared with the Q-Body coil, consistent with findings from previous studies using cylindrical quadrature coils [32] and (phased array) surface coils [33, 34]. This difference may be attributed to the non-uniform and relatively small sensitivity area of each phased array coil element (Fig. 11), which effectively reduces the impact of object anisotropy, while the Q-Body coil has a uniform sensitivity throughout the entire anisotropic object. Nevertheless, the phased array coil still showed a positive effect for anisotropic FOV because, despite the non-uniformity, each coil element is still sensitive to a major part of the object (particularly the central elements). Moreover, the contours of constant sensitivity for each coil element are anisotropic in planes perpendicular to the coil [57], with their larger dimensions aligned parallel to the major axis of the scanned object in axial imaging. This is also relevant for 3DPR with selective excitation and anisotropic unaliased FOV in the slice direction. When the excited 3D volume thickness is relatively thin (roughly equal or smaller than the coil element size in that direction), applying an anisotropic, oblate unaliased FOV can be beneficial [32, 34].

Anisotropic FOV and undersampling

The effectiveness of anisotropic FOV may depend on the level of undersampling. At low undersampling levels, reducing the minor axis unaliased FOV decreases scan time without increasing the level of radial aliasing (for objects with matching anisotropic in-plane dimensions), while at higher undersampling, tailoring the unaliased FOV using the same scan time reduces the level of radial aliasing, as previously reported by Larson et al. [32]. As shown in Fig. 9, the overall reduction in aliasing artifact level of ASOS compared with conventional SOS using identical scan time SOS'^{a} was fairly pronounced at lower undersampling levels (large ρ_0), while it appeared less pronounced at higher undersampling levels (smaller ρ_0). This is to be expected, because for ASOS with low undersampling, the corresponding SOS'^{a} oversampled the object in the vertical direction, while for ASOS with higher undersampling, the corresponding SOS'^{a} undersampled the object in this direction. However, even for the higher undersampling, ASOS still showed some benefits compared to the corresponding SOS'^{a}. This result is in line with earlier studies, which found benefits of anisotropic FOV even in the case of highly undersampled radial acquisitions, for 2D [33] and 3DPR [32, 34].

Acceleration techniques

Radial parallel imaging [58–60], radial compressed sensing [8, 20, 61–65], and deep learning-based reconstructions [66, 67] might be combined with variable density and anisotropic in-plane FOV SOS. Whereas the potential benefits of anisotropic in-plane FOV for these radial acceleration techniques still need to be investigated, variable density has already shown benefits for radial compressed sensing [29]. Cartesian compressed sensing commonly employs variable density random undersampling, with a lower sampling density at the periphery of k-space than at the center [69]. Variable density SOS results in a decreasing radial sampling density towards the periphery of k_z, and is thus beneficial for compressed sensing. This has already been demonstrated using a density step function for VSOS [29]. Sampling incoherence in the k_z direction also benefits compressed sensing, and this can be obtained with rotated SOS [53] or with a variable density of k_z planes [68]. Additionally, combining an elliptical k-space shutter with compressed sensing (using $S(k_z) > D_v(k_z)$) may be beneficial because it could reduce image noise without compromising spatial resolution.

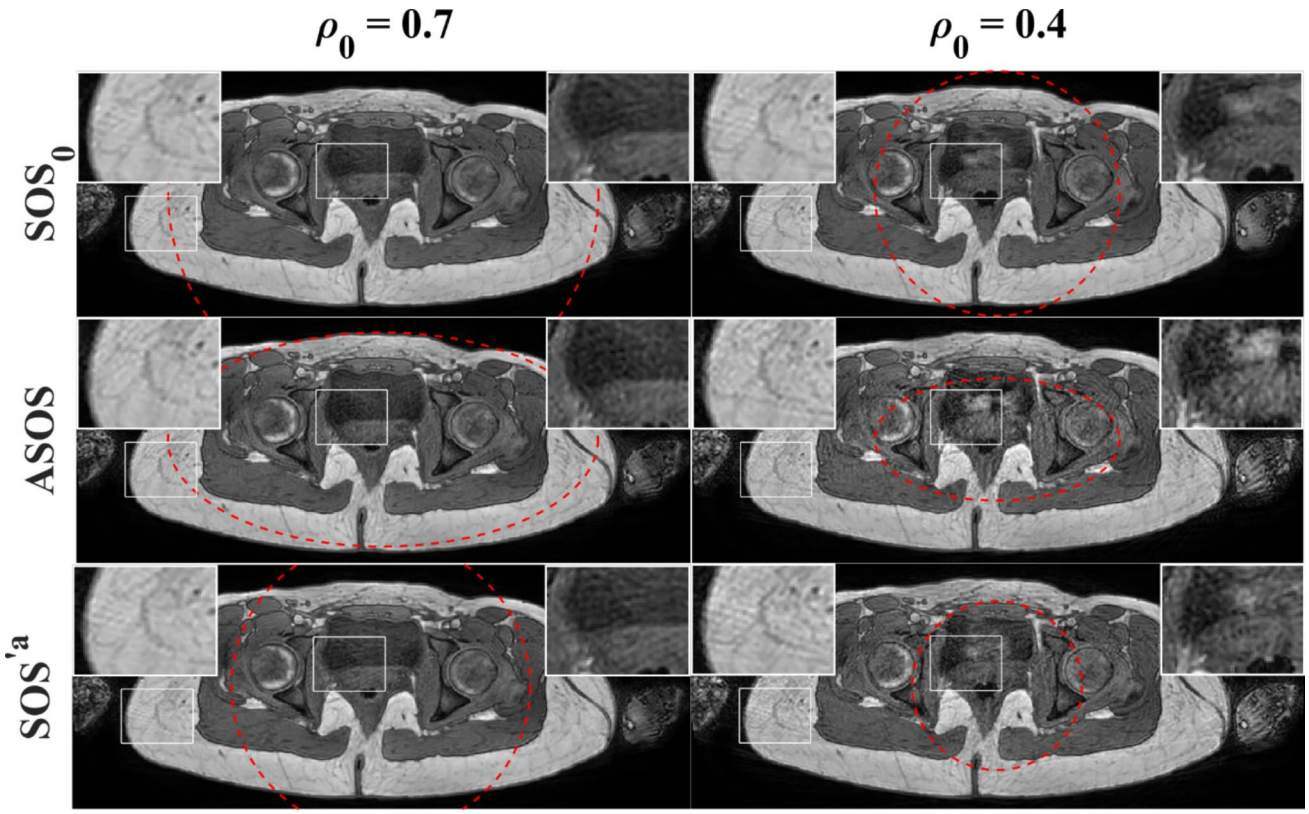

Fig. 9 Pelvic images comparing sampling factors $\rho_0 = 0.7$ (left column,) and $\rho_0 = 0.4$ (right column) for conventional SOS (SOS_0) and ASOS acquisitions, using the phased array coil. SOS'^a was retrospectively undersampled from SOS_0. The red dashed lines indicate the size and shape of the uFOV. ASOS (middle row) had a 31% shorter scan time than SOS_0 (top row), while having the same (major axis) uFOV size. SOS'^a (bottom row) had the same scan time as ASOS, while having a 31% smaller uFOV ($\rho' = 0.69$) than SOS_0. The images in the left column are identical to the corresponding images in Fig. 7. To better illustrate the aliasing artifacts, certain regions (white rectangles) are enlarged in the inset

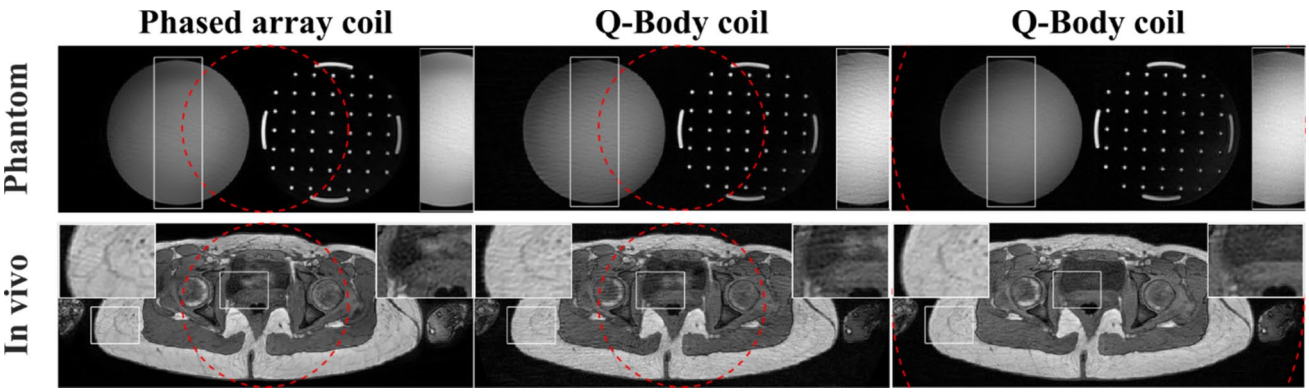

Fig. 10 Phantom (top row) and pelvic (bottom row) images obtained using conventional SOS with different coils and unaliased FOV (uFOV) sizes. The red dashed lines indicate the uFOV size. Phased array coil (left column, $\rho = 0.4$), Q-Body coil with the same uFOV (middle column, $\rho = 0.4$), and Q-Body coil with 2.5-fold larger uFOV (right column, $\rho = 1$). To compensate for the lower SNR with the Q-Body coil, NSA = 5 was used for $\rho = 0.4$, and NSA = 2 for $\rho = 1$. To better illustrate the aliasing artifacts, certain regions (white rectangles) are enlarged in the inset

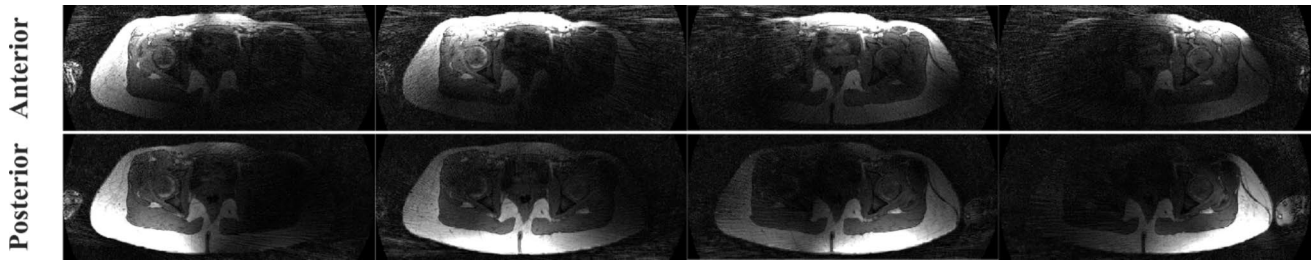

Fig. 11 Eight single-element images from the phased array coil. Four anterior coil elements (top row) and four posterior coil elements (bottom row) are displayed. Pelvic imaging was performed in axial orientation using conventional SOS (SOS_0 acquisition from Fig. 7)

The effects of anisotropic FOV on image quality can be fairly subtle, and aliasing artifacts may be partly visible as pseudo-noise. To investigate the effects with sufficiently high SNR, our study only used through-plane acceleration, with a moderate acceleration factor of 2 for the phased array coil. For the Q-Body coil, even without acceleration, 2–5 signal averages were necessary to be able to properly study the effects. Also, at the time of our study, in-plane radial acceleration reconstruction techniques were not yet available on the scanner.

Furthermore, compressed sensing with radial undersampling has high computational demands for reconstruction [20, 21, 69], while VASOS provides an alternative method for acceleration with a reduction factor of almost 2, without an increase in computational demand.

Although our study did not include radial in-plane acceleration techniques, it provides relevant insights into the effects of radial undersampling and it is the first to evaluate the benefits of anisotropic FOV for SOS. Additionally, our newly developed analytical expressions for elliptical FOV radial profile angles - with and without golden angle - will facilitate future studies in assessing the potential benefits of anisotropic FOV for radial imaging with in-plane acceleration techniques.

Conclusions

The effectiveness of variable density and anisotropic FOV was evaluated for 3D Stack-Of-Stars radial imaging using an elliptical variable density function and an elliptical in-plane uFOV with a major-to-minor-axis ratio of 1:0.5. The impact of receiver coil on the effectiveness of these techniques was also studied by comparing a phased array coil with the quadrature body coil.

Compared with conventional SOS, variable density reduced scan time by 20% while maintaining comparable levels of radial aliasing artifacts. Anisotropic FOV decreased scan time by 31%, achieving similar radial aliasing artifact levels at low undersampling, for objects with matching in-plane anisotropy. Combining both techniques resulted in a 45% scan time reduction. Alternatively, when comparing with conventional SOS using identical scan time, variable density and anisotropic FOV both reduced the radial aliasing artifact level, albeit less pronounced at higher undersampling for anisotropic FOV.

All these results were observed for both the Q-Body coil and the phased array coil, even though the phased array coil generally resulted in a lower aliasing artifact level than the Q-Body coil. The benefits of variable density were independent of the used coil, while the benefits of anisotropic FOV were less pronounced with the phased array coil.

We have presented new analytic expressions to compute the profile angles for radial imaging with an elliptical uFOV, including golden angle sampling. This will facilitate future studies on radial imaging with anisotropic FOV, including in-plane acceleration techniques.

Appendix

Profile density D_{va}, relative scan time T_{va} and number of profiles N_{tva} for VASOS

The variable, anisotropic radial profile density for VASOS (D_{va}) is a function of k_z, η and θ, and is the product of D_v and D_a:

$$D_{va}\left(k_z,\eta,\theta\right) = D_v\left(k_z\right)\cdot D_a(\eta,\theta) \tag{27}$$

The relative scan time for VASOS (T_{va}) is defined as $T_{va} = \frac{1}{R_{va}} = \frac{N_{tva}}{N_{tc}} = \overline{D}_{va}$, where N_{tva} is the total number of VASOS profiles, and $\overline{D}_{va}$ the average density (D_{va} averaged over both k_z and θ). Because D_v and D_a are independent functions, $\overline{D}_{va} = \overline{D}_v \cdot \overline{D}_a$, and T_{va} can be expressed as:

$$T_{va}\left(f_p,\eta\right) = T_v\left(f_p\right)\cdot T_a(\eta) \tag{28}$$

where $0 < T_{va} \leq \frac{4}{\pi}$. T_v and T_a are given by Eqs. 6 and 10, respectively. For an elliptical uFOV, $T_{va} \leq 1$. For a circular uFOV, and without variable density, $T_{va}\left(f_p,1\right) = 1$.

The total number of acquired profiles with VASOS is $N_{tva}(f_p,\eta) = N_z \cdot N_{\theta c} \cdot T_{va}(f_p,\eta)$. With Eq. 2, this can be written as:

$$N_{tva}(f_p,\eta) = \frac{N_z \cdot N_r \cdot \pi}{2} \cdot \rho \cdot T_{va}(f_p,\eta) \tag{29}$$

where the radial sampling factor $\rho = uFOV_c/FOV_r = uFOV_a^+/FOV_r$ (using Eq. 7).

Profile angles θ_i for elliptical FOV

Wu et al. [33] used the iterative method from Larson et al. [32] to compute the radial profile angles θ for anisotropic uFOV for 2D imaging. They also already noticed that the angle θ_i of the i^{th} radial profile is determined by the integral from 0 to θ_i of the anisotropic profile density, which is proportional to the number of profiles in that range. For each k_z partition in VASOS, with a linear profile order, this means that $\int_0^{\theta_i} D_{va}(k_z,\eta,\theta)\,d\theta \propto i$. With Eq. 27, this can be expressed as:

$$\int_0^{\theta_i} D_a(\eta,\theta)\,d\theta = \frac{i}{N_{\theta va}(k_z,\eta)} \cdot \int_0^{\pi} D_a(\eta,\theta)\,d\theta \tag{30}$$

where $i = 0,1,2,\ldots,N_{\theta va}(k_z,\eta) - 1, \theta_0 = 0$, and $0 \le \theta_i < \pi$ (by definition, $\theta_{N_{\theta va}(k_z,\eta)} = \pi$). θ_i depends on k_z and η ($\theta_i = \theta(i,k_z,\eta)$), but for simplicity, this is not included in the notation. To solve Eq. 30 for θ_i, the density function D_a (and corresponding $uFOV_a$ shape) needs to be defined.

Using Eq. 15 for the density D_a of an elliptical $uFOV_a$, the incomplete elliptic integral of the first kind $F(\varphi,k)$, and $\eta' = \sqrt{1-\eta^2}$, Eq. 30 can be rewritten as:

$$F(\theta_i,\eta') = u_i \tag{31}$$

where, using the identity $F(\pi,k) \equiv 2K(k)$, u_i is defined as:

$$u_i = \frac{i}{N_{\theta va}(k_z,\eta)} \cdot 2K(\eta') \tag{32}$$

The solution for θ_i in Eq. 31 can be expressed analytically by means of the Jacobi elliptic amplitude function $\mathrm{am}(u,k)$:

$$\theta_i = \mathrm{am}(u_i,\eta') \tag{33}$$

$\hat{u}_i^*$ for elliptical FOV with pseudo golden angle

For pseudo golden angle sampling [9–11], $\hat{u}_i$ in Eq. 20 is defined as:

$$\hat{u}_i^* = \frac{\mathrm{round}\left(N_{\theta va}(k_z,\eta) \cdot \frac{i}{\tau}\right)}{N_{\theta va}(k_z,\eta)} \cdot 2K(\eta') \tag{34}$$

For a circular uFOV ($\eta = 1, \eta' = 0$), Eqs. 20 and 34 reduce to $\hat{\theta}_i^* = \hat{u}_i^* = \frac{\mathrm{round}\left(N_{\theta v}(k_z) \cdot i/\tau\right)}{N_{\theta v}(k_z)} \cdot \pi$ for VSOS, and for conventional SOS they reduce to $\hat{\theta}_i^* = \hat{u}_i^* = \frac{\mathrm{round}\left(N_{\theta c} \cdot i/\tau\right)}{N_{\theta c}} \cdot \pi$, which are the angles for conventional pseudo golden angle sampling.

Acknowledgements This work was supported by the European Commission within the Horizon 2020 Framework through the MSCA-ITN-ETN European Training Networks (project number 642458). The authors would like to thank Dr. Gabrielle Beck, Dr. Hans Peeters and Prof. Dr. Peter Börnert for helpful discussions.

Author contributions Joao Tourais: Study conception and design, Acquisition of data, Analysis and interpretation of data, Drafting of manuscript, Critical revision. Guruprasad Krishnamoorthy: Critical revision. Jouke Smink: Critical revision. Marcel Breeuwer: Critical revision. Marc Kouwenhoven: Study conception and design, Acquisition of data, Analysis and interpretation of data, Drafting of manuscript, Critical revision.

Funding Horizon 2020 Framework Programme, 642458, Marcel Breeuwer.

Data availability The data that support the findings of this study are not openly available due to reasons of sensitivity and are available from the corresponding author upon reasonable request.

Declarations

Conflict of interest Jouke Smink and Marc Kouwenhoven are employees of Philips Medical Systems B.V.

Ethical approval This study was conducted in accordance with the ethical standards of the 1964 Declaration of Helsinki and its later amendments. Approval was obtained from the appropriate institutional review board.

Informed consent Informed consent was obtained from all participants.

References

1. Glover GH, Pauly JM (1992) Projection reconstruction techniques for reduction of motion effects in MRI. Magn Reson Med 28(2):275–289
2. Chandarana H, Block TK, Rosenkrantz AB, Lim RP, Kim D, Mossa DJ, Babb JS, Kiefer B, Lee VS (2011) Free-breathing radial 3D fat-suppressed T1-weighted gradient echo sequence: a viable alternative for contrast-enhanced liver imaging in patients unable to suspend respiration. Invest Radiol 46(10):648–653
3. Reiner CS, Neville AM, Nazeer HK, Breault S, Dale BM, Merkle EM, Bashir MR (2013) Contrast-enhanced free-breathing 3D T1-weighted gradient-echo sequence for hepatobiliary MRI in patients with breath-holding difficulties. Eur Radiol 23(11):3087–3093
4. Peters DC, Korosec FR, Grist TM, Block WF, Holden JE, Vigen KK, Mistretta CA (2000) Undersampled projection reconstruction applied to MR angiography. Magn Reson Med 43(1):91–101
5. Peters DC, Ennis DB, Rohatgi P, Syed MA, McVeigh ER, Arai AE (2004) 3D breath-held cardiac function with projection reconstruction in steady state free precession validated using 2D cine MRI. J Magn Reson Imaging 20(3):411–416
6. Larson AC, Simonetti OP, Li D (2002) Coronary MRA with 3D undersampled projection reconstruction TrueFISP. Magn Reson Med 48(4):594–601
7. Liu J, Spincemaille P, Codella NC, Nguyen TD, Prince MR, Wang Y (2010) Respiratory and cardiac self-gated free-breathing cardiac CINE imaging with multiecho 3D hybrid radial SSFP acquisition. Magn Reson Med 63(5):1230–1237
8. Chandarana H, Feng L, Block TK, Rosenkrantz AB, Lim RP, Babb JS, Sodickson DK, Otazo R (2013) Free-breathing contrast-enhanced multiphase MRI of the liver using a combination of compressed sensing, parallel imaging, and golden-angle radial sampling. Invest Radiol 48(1):10–16
9. Hedderich DM, Weiss K, Spiro JE, Giese D, Beck GM, Maintz D, Persigehl T (2018) Clinical evaluation of free-breathing contrast-enhanced T1w MRI of the liver using pseudo golden angle radial k-space sampling. Rofo 190(7):601–609
10. Kim YC, Min JH, Kim YK, Lee SJ, Ahn S, Kim E, Peeters H (2019) Intra-individual comparison of gadolinium-enhanced MRI using pseudo-golden-angle radial acquisition with gadoxetic acid-enhanced MRI for diagnosis of HCCs using LI-RADS. Eur Radiol 29(4):2058–2068
11. Kajita K, Goshima S, Noda Y, Kawada H, Kawai N, Okuaki T, Honda M, Matsuo M (2019) Thin-slice free-breathing pseudo-golden-angle radial stack-of-stars with gating and tracking T1-weighted acquisition: an efficient gadoxetic acid-enhanced hepatobiliary-phase imaging alternative for patients with unstable breath holding. Magn Reson Med Sci 18(1):4–11
12. Rosenkrantz AB, Geppert C, Grimm R, Block TK, Glielmi C, Feng L, Otazo R, Ream JM, Romolo MM, Taneja SS, Sodickson DK, Chandarana H (2015) Dynamic contrast-enhanced MRI of the prostate with high spatiotemporal resolution using compressed sensing, parallel imaging, and continuous golden-angle radial sampling: preliminary experience. J Magn Reson Imaging 41(5):1365–1373
13. Li Y, Xia C, Peng W, Gao Y, Hu S, Zhang K, Zhao F, Benkert T, Zhou X, Zhang H, Li Z (2020) Dynamic contrast-enhanced MR imaging of rectal cancer using a golden-angle radial stack-of-stars VIBE sequence: comparison with conventional contrast-enhanced 3D VIBE sequence. Abdom Radiol (NY) 45(2):322–331
14. Winkelmann S, Schaeffter T, Koehler T, Eggers H, Doessel O (2007) An optimal radial profile order based on the golden ratio for time-resolved MRI. IEEE Trans Med Imaging 26(1):68–76
15. Feng L (2022) Golden-angle radial MRI: basics, advances, and applications. J Magn Reson Imaging 56(1):45–62
16. Pruessmann KP, Weiger M, Scheidegger MB, Boesiger P (1999) SENSE: sensitivity encoding for fast MRI. Magn Reson Med 42(5):952–962
17. Griswold MA, Jakob PM, Heidemann RM, Nittka M, Jellus V, Wang J, Kiefer B, Haase A (2002) Generalized autocalibrating partially parallel acquisitions (GRAPPA). Magn Reson Med 47(6):1202–1210
18. McGibney G, Smith MR, Nichols ST, Crawley A (1993) Quantitative evaluation of several partial Fourier reconstruction algorithms used in MRI. Magn Reson Med 30(1):51–59
19. Vigen KK, Peters DC, Grist TM, Block WF, Mistretta CA (2000) Undersampled projection-reconstruction imaging for time-resolved contrast-enhanced imaging. Magn Reson Med 43(2):170–176
20. Block KT, Uecker M, Frahm J (2007) Undersampled radial MRI with multiple coils. Iterative image reconstruction using a total variation constraint. Magn Reson Med 57(6):1086–1098
21. Block KT, Chandarana H, Milla S, Bruno M, Mulholland T, Fatterpekar G, Hagiwara M, Grimm R, Geppert C, Kiefer B, Sodickson DK (2014) Towards routine clinical use of radial stack-of-stars 3D gradient-echo sequences for reducing motion sensitivity. J Korean Soc Magn Reson Med 18(2):87–106
22. Peters DC, Nezafat R, Manning WJ (2007) Radial undersampling that is variable in Kz. In: Proceedings of the 16th scientific meeting, International Society for Magnetic Resonance in medicine, Berlin, Germany, pp. 304
23. Bhat H, Yang Q, Zuehlsdorff S, Li K, Li D (2011) Contrast-enhanced whole-heart coronary magnetic resonance angiography at 3 T with radial EPI. Magn Reson Med 66(1):82–91
24. Endler CH, Kukuk GM, Peeters JM, Beck GM, Isaak A, Faron A, Mesropyan N, Luetkens JA, Attenberger UI, Kupczyk PA (2022) Dynamic liver magnetic resonance imaging during free breathing: a feasibility study with a motion compensated variable density radial acquisition and a viewsharing high-pass filtering reconstruction. Invest Radiol 57(7):470–477
25. Wu C, Peng Q, Jafari R, Zhao Y, Yu V, Otazo R (2023) Fast free-breathing 3D T1ρ abdominal imaging using an efficient diamond radial sampling strategy at 3T. In: Proceedings of the 31st scientific meeting, International Society for Magnetic Resonance in medicine, Toronto, Canada, pp. 1848.
26. Spogis J, Katemann C, Zhang S, Esser M, Tsiflikas I, Schafer J (2023) Feasibility and implementation of a 4D free-breathing variable density stack-of-stars functional magnetic resonance urography in young children without sedation. Invest Radiol 59(3):271–277
27. Berman BP, Li Z, Altbach MI, Galons JP, Martin DR, Dong B, Sharma P, Kalb BT, Bilgin A. (2013) How to stack the stars: a variable center-dense k-space trajectory for 3D MRI. In: Proceedings of the 21st Annual Meeting of ISMRM; Salt Lake City, UT, USA. pp. 3829.
28. Li Z, Berman BP, Altbach MI, Galons JP, Martin DR, Dong B, Sharma P, Raghunand N, Bilgin A (2013) Highly accelerated 3D dynamic imaging with variable density golden angle stack-of-stars sampling. In: Proceedings of the 21st Annual Meeting of ISMRM Salt Lake City, UT, USA. pp. 3797.
29. Haji-Valizadeh H, Collins JD, Aouad PJ, Serhal AM, Lindley MD, Pang J, Naresh NK, Carr JC, Kim D (2019) Accelerated, free-breathing, noncontrast, electrocardiograph-triggered, thoracic MR angiography with stack-of-stars k-space sampling and GRASP reconstruction. Magn Reson Med 81(1):524–532
30. Scheffler K, Hennig J (1998) Reduced circular field-of-view imaging. Magn Reson Med 40(3):474–480
31. Scheffler K (1999) Tomographic imaging with nonuniform angular sampling. J Comput Assist Tomogr 23(1):162–166

32. Larson PZ, Gurney PT, Nishimura DG (2008) Anisotropic field-of-views in radial imaging. IEEE Trans Med Imaging 27(1):47–57
33. Wu Z, Han F, Hu P, Nayak KS (2016) Anisotropic field-of-view support for golden angle radial imaging. Magn Reson Med 76(1):229–236
34. Krishnamoorthy G, Smink J, Tourais J, Breeuwer M, Kouwenhoven M (2021) Variable anisotropic FOV for 3D radial imaging with spiral phyllotaxis (VASP). Magn Reson Med 85(1):68–77
35. Han M, Larson PE, Liu J, Krug R (2014) Depiction of Achilles tendon microstructure in vivo using high-resolution 3-dimensional ultrashort echo-time magnetic resonance imaging at 7 T. Invest Radiol 49(5):339–345
36. Ding Z, Cheng Z, She H, Liu B, Yin Y, Du YP (2022) Dynamic pulmonary MRI using motion-state weighted motion-compensation (MostMoCo) reconstruction with ultrashort TE: a structural and functional study. Magn Reson Med 88(1):224–238
37. Pipe JG (2000) Reconstructing MR images from undersampled data: data-weighting considerations. Magn Reson Med 43(6):867–875
38. Lauzon ML, Rutt BK (1996) Effects of polar sampling in k-space. Magn Reson Med 36(6):940–949
39. Barger AV, Peters DC, Block WF, Vigen KK, Korosec FR, Grist TM, Mistretta CA (2000) Phase-contrast with interleaved undersampled projections. Magn Reson Med 43(4):503–509
40. Boost C++ Libraries. https://www.boost.org/. Accessed May 6, 2023.
41. Schomberg H, Timmer J (1995) The gridding method for image reconstruction by Fourier transformation. IEEE Trans Med Imaging 14(3):596–607
42. Rasche V, Proksa R, Sinkus R, Bornert P, Eggers H (1999) Resampling of data between arbitrary grids using convolution interpolation. IEEE Trans Med Imaging 18(5):385–392
43. Roemer PB, Edelstein WA, Hayes CE, Souza SP, Mueller OM (1990) The NMR phased array. Magn Reson Med 16(2):192–225
44. Buehrer M, Pruessmann KP, Boesiger P, Kozerke S (2007) Array compression for MRI with large coil arrays. Magn Reson Med 57(6):1131–1139
45. van den Brink JS, Watanabe Y, Kuhl CK, Chung T, Muthupillai R, Van Cauteren M, Yamada K, Dymarkowski S, Bogaert J, Maki JH, Matos C, Casselman JW, Hoogeveen RM (2003) Implications of SENSE MR in routine clinical practice. Eur J Radiol 46(1):3–27
46. Willinek WA, Gieseke J, Kukuk GM, Nelles M, Konig R, Morakkabati-Spitz N, Traber F, Thomas D, Kuhl CK, Schild HH (2010) Dual-source parallel radiofrequency excitation body MR imaging compared with standard MR imaging at 3.0 T: initial clinical experience. Radiology 256(3):966–975
47. Nehrke K, Bornert P (2012) DREAM–a novel approach for robust, ultrafast, multislice B(1) mapping. Magn Reson Med 68(5):1517–1526
48. Wundrak S, Paul J, Ulrici J, Hell E, Rasche V (2015) A small surrogate for the golden angle in time-resolved radial MRI based on generalized Fibonacci sequences. IEEE Trans Med Imaging 34(6):1262–1269
49. Wundrak S, Paul J, Ulrici J, Hell E, Geibel MA, Bernhardt P, Rottbauer W, Rasche V (2016) Golden ratio sparse MRI using tiny golden angles. Magn Reson Med 75(6):2372–2378
50. Bernstein MA, Fain SB, Riederer SJ (2001) Effect of windowing and zero-filled reconstruction of MRI data on spatial resolution and acquisition strategy. J Magn Reson Imaging 14(3):270–280
51. Irarrazabal P, Nishimura DG (1995) Fast three dimensional magnetic resonance imaging. Magn Reson Med 33(5):656–662
52. Thedens DR, Irarrazaval P, Sachs TS, Meyer CH, Nishimura DG (1999) Fast magnetic resonance coronary angiography with a three-dimensional stack of spirals trajectory. Magn Reson Med 41(6):1170–1179
53. Zhou Z, Han F, Yan L, Wang DJJ, Hu P (2017) Golden-ratio rotated stack-of-stars acquisition for improved volumetric MRI. Magn Reson Med 78(6):2290–2298
54. Pusey E, Yoon C, Anselmo ML, Lufkin RB (1988) Aliasing artifacts in MR imaging. Comput Med Imaging Graph 12(4):219–224
55. Blaimer M, Breuer F, Mueller M, Heidemann RM, Griswold MA, Jakob PM (2004) SMASH, SENSE, PILS, GRAPPA: how to choose the optimal method. Top Magn Reson Imaging 15(4):223–236
56. Griswold MA, Jakob PM, Nittka M, Goldfarb JW, Haase A (2000) Partially parallel imaging with localized sensitivities (PILS). Magn Reson Med 44(4):602–609
57. Schenck JF, Hart HR, Jr., Foster TH, Edelstein WA, Hussain MA (1986) High resolution magnetic resonance imaging using surface coils. Magn Reson Annu 123–160.
58. Pruessmann KP, Weiger M, Bornert P, Boesiger P (2001) Advances in sensitivity encoding with arbitrary k-space trajectories. Magn Reson Med 46(4):638–651
59. Seiberlich N, Breuer FA, Ehses P, Moriguchi H, Blaimer M, Jakob PM, Griswold MA (2009) Using the GRAPPA operator and the generalized sampling theorem to reconstruct undersampled non-Cartesian data. Magn Reson Med 61(3):705–715
60. Wright KL, Hamilton JI, Griswold MA, Gulani V, Seiberlich N (2014) Non-cartesian parallel imaging reconstruction. J Magn Reson Imaging 40(5):1022–1040
61. Adluru G, Chen L, Kim SE, Burgon N, Kholmovski EG, Marrouche NF, Dibella EV (2011) Three-dimensional late gadolinium enhancement imaging of the left atrium with a hybrid radial acquisition and compressed sensing. J Magn Reson Imaging 34(6):1465–1471
62. Feng L, Grimm R, Block KT, Chandarana H, Kim S, Xu J, Axel L, Sodickson DK, Otazo R (2014) Golden-angle radial sparse parallel MRI: combination of compressed sensing, parallel imaging, and golden-angle radial sampling for fast and flexible dynamic volumetric MRI. Magn Reson Med 72(3):707–717
63. Wech T, Pickl W, Tran-Gia J, Ritter C, Beer M, Hahn D, Kostler H (2014) Whole-heart cine MRI in a single breath-hold–a compressed sensing accelerated 3D acquisition technique for assessment of cardiac function. Rofo 186(1):37–41
64. Feng L, Axel L, Chandarana H, Block KT, Sodickson DK, Otazo R (2016) XD-grasp: golden-angle radial MRI with reconstruction of extra motion-state dimensions using compressed sensing. Magn Reson Med 75(2):775–788
65. Feng L, Huang C, Shanbhogue K, Sodickson DK, Chandarana H, Otazo R (2018) RACER-GRASP: respiratory-weighted, aortic contrast enhancement-guided and coil-unstreaking golden-angle radial sparse MRI. Magn Reson Med 80(1):77–89
66. Lv J, Chen K, Yang M, Zhang J, Wang X (2018) Reconstruction of undersampled radial free-breathing 3D abdominal MRI using stacked convolutional auto-encoders. Med Phys 45(5):2023–2032
67. Jafari R, Do RKG, LaGratta MD, Fung M, Bayram E, Cashen T, Otazo R (2023) GrasPNet: fast spatiotemporal deep learning reconstruction of golden-angle radial data for free-breathing dynamic contrast-enhanced magnetic resonance imaging. NMR Biomed 36(3):e4861
68. Li Z, Huang C, Tong A, Chandarana H, Feng L (2023) Kz-accelerated variable-density stack-of-stars MRI. Magn Reson Imaging 97:56–67
69. Lustig M, Donoho D, Pauly JM (2007) Sparse MRI: the application of compressed sensing for rapid MR imaging. Magn Reson Med 58(6):1182–1195